



Compact high order finite volume method on unstructured grids III: Variational reconstruction



Qian Wang^a, Yu-Xin Ren^{a,*}, Jianhua Pan^a, Wanai Li^b

^a Department of Engineering Mechanics, Tsinghua University, Beijing 100084, China

^b Sino-French Institute of Nuclear Engineering & Technology, Sun Yat-Sen University, Zhuhai 519082, China

ARTICLE INFO

Article history:

Received 15 October 2016

Received in revised form 25 January 2017

Accepted 10 February 2017

Available online 20 February 2017

Keywords:

Variational reconstruction

Interfacial jump integration

Reconstruction and time integration

coupled iteration method

High order finite volume method

Unstructured grids

ABSTRACT

This paper presents a variational reconstruction for the high order finite volume method in solving the two-dimensional Navier–Stokes equations on arbitrary unstructured grids. In the variational reconstruction, an interfacial jump integration is defined to measure the jumps of the reconstruction polynomial and its spatial derivatives on each cell interface. The system of linear equations to determine the reconstruction polynomials is derived by minimizing the total interfacial jump integration in the computational domain using the variational method. On each control volume, the derived equations are implicit relations between the coefficients of the reconstruction polynomials defined on a compact stencil involving only the current cell and its direct face-neighbors. The reconstruction and time integration coupled iteration method proposed in our previous paper is used to achieve high computational efficiency. A problem-independent shock detector and the WBAP limiter are used to suppress non-physical oscillations in the simulation of flow with discontinuities. The advantages of the finite volume method using the variational reconstruction over the compact least-squares finite volume method proposed in our previous papers are higher accuracy, higher computational efficiency, more flexible boundary treatment and non-singularity of the reconstruction matrix. A number of numerical test cases are solved to verify the accuracy, efficiency and shock-capturing capability of the finite volume method using the variational reconstruction.

© 2017 Elsevier Inc. All rights reserved.

1. Introduction

The large reconstruction stencil has been the major bottleneck problem in developing high order finite volume method on unstructured grids. A compact high order finite volume method on unstructured grids, termed as the compact least-squares finite volume (CLSFV) method, has been developed by Wang et al. [1,2] for one and two-dimensional Euler equations recently to overcome this shortcoming. In the present paper, an improved reconstruction procedure based on compact stencil is proposed for the high order finite volume method solving two-dimensional Euler and Navier–Stokes equations on arbitrary unstructured grids.

Over the last two decades, various high order methods with compact stencils on unstructured grids have been developed, such as the discontinuous Galerkin (DG) method [3–7], $P_N P_M$ procedure [8–10], RDG method [11,12], DG/FV method [13,14], Residual Distribution (RD) method [15–18], spectral volume (SV) [19–22] / spectral difference (SD) [23–25] methods and

* Corresponding author.

E-mail address: ryx@tsinghua.edu.cn (Y.-X. Ren).

correction procedure via reconstruction (CPR) method [26,27]. A common feature of these methods is that they can achieve high order accuracy on a compact stencil involving only the current cell and its face-neighboring cells (the von Neumann neighbors). This is the fundamental advantage of these methods over the traditional high order finite volume (FV) methods, such as the k -exact [28–31] / WENO [32–35] FV methods, which require large stencils to reconstruct high order polynomial distributions within a typical control volume. The CLSFV method is an improvement of the traditional FV schemes, which, similar to the DG, SV, SD and CPR methods, can achieve arbitrary high order accuracy using a compact stencil consisting of the cell of interest and its von Neumann neighbors.

The key element of the CLSFV method is the compact least-squares (CLS) reconstruction. The polynomial of the CLS reconstruction is determined by conserving the cell averages of the solution and its various order of derivatives on the face-neighboring cells for sufficiently smooth solution. Compared with the traditional reconstructions that only require the conservation of the solution, the conservation of various orders of derivatives in the CLS reconstruction provides additional constitutive relations so that the reconstruction can be performed on a compact stencil. The CLS reconstruction is implicit. In multi-dimensional cases, the CLS reconstruction results in a large sparse linear equation system for which both direct and iterative solvers are computationally very expensive. A reconstruction and time integration coupled iteration method is proposed in [2] for the CLSFV method to achieve high computational efficiency. Numerical results demonstrate the CLSFV method is more accurate and efficient in terms of the CPU time to reach the same accuracy than the traditional k -exact FV method in the framework of implicit time stepping [2]. The main shortcoming of the CLS reconstruction is that the reconstruction polynomials at the control volumes close to the boundary should be one order lower than those at the inner control volumes, which reduces the accuracy of the scheme near the boundary. Furthermore, similar to the k -exact reconstruction [28], the system of the linear equations of the CLS reconstruction may be singular. Although this difficulty is not encountered frequently in practical applications, it does indicate the non-robustness of the CLS reconstruction in certain cases. These considerations motivate the proposal of the variational reconstruction in the present paper.

The variational reconstruction represents a new class of reconstruction procedures for high order finite volume schemes on unstructured grids. This approach is mainly motivated by the success of the CLS reconstructions proposed in our previous paper [2] in which we showed that implicit reconstructions on the compact stencil could be solved efficiently if they are coupled properly with implicit time integrations. The variational reconstruction is a general approach to design the implicit reconstruction. The key element of the variational reconstruction is the cost function that should be properly designed to make the resulting reconstruction procedure compact and accurate.

In the present paper, a specific variational reconstruction is studied in detail, in which an interfacial jump integration (IJI) is defined to measure the jumps of the reconstruction polynomial and its spatial derivatives on each cell interface. The cost function is the summation of the IJI over the entire computational domain. The reconstruction procedure is derived by the minimization of the total IJI. This procedure produces a system of linear equations. Therefore, the reconstruction is implicit. Furthermore, the system of linear equations is sparse in the sense that the equations on each control volume only involve information defined on the current and face-neighboring control volumes. Therefore, this reconstruction procedure is compact. In practice, the linear equation system is solved iteratively using the reconstruction and time integration coupled iteration method proposed in [2] to achieve high computational efficiency.

The FV method using the variational reconstruction, which is the variational FV (VfV) method in the present paper, is more accurate and efficient than the CLSFV method. The reconstruction polynomial of the variational reconstruction is obtained by the minimization of the jumps of the depended variable and its spatial derivatives across the cell interfaces. The reduction of the jump of the dependent variables is beneficial for the reduction of numerical viscosity and the reduction of the jump of the first derivatives is beneficial for the accuracy of the viscous flux computation. The Fourier analysis in one-dimensional case indicates that the VfV scheme has smaller dispersion and dissipation errors than the CLSFV scheme. The numerical results of two-dimensional test cases show that the VfV method has higher accuracy and efficiency than the CLSFV method. In [36], Sun et al. found that reconstructions with smaller boundary variation (BV) are less dissipative and generate solutions with higher accuracy and resolution for inviscid flow problems. The IJI defined in the present paper can be regarded as a generalized BV including not only the BV of the dependent variables but also the BV of their derivatives. Therefore, the minimization of the total IJI provides a general principle to design low dissipation schemes.

The boundary treatment of the VfV method is more flexible than the CLSFV method. In multi-dimensional CLS reconstruction, the reconstruction at boundary cells must be one-order lower in accuracy than the reconstruction at inner cells because there are not enough constitutive equations. On the other hand, the variational reconstruction always provides enough information so that there is no need to reduce the reconstruction accuracy at physical boundaries. Furthermore, the boundary conditions are much easier to be implemented in the variational reconstruction than the CLS reconstruction. For example, the CLS reconstruction needs to introduce techniques such as the constrained least-squares [31] to treat the non-slip solid wall boundary condition, while the variational reconstruction only needs to add boundary jump integration terms to the total IJI. Therefore, the VfV method has more accurate and flexible boundary treatment capability than the CLSFV method.

Another significant improvement of the VfV method over the CLSFV method is the non-singularity of the reconstruction matrix. The variational reconstruction corresponds to a global minimization problem. The resulting reconstruction matrix is symmetric and positive definite, which guarantees that the reconstruction matrix is invertible, i.e., the linear equation system is solvable. We can always obtain a piece-wise polynomial solution distribution via the variational reconstruction, which is a significant advantage over the CLS and k -exact reconstructions. For the CLS reconstruction, we can not prove

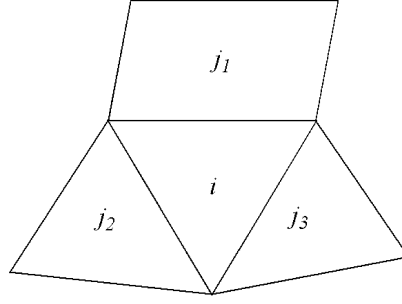


Fig. 1. Reconstruction stencil for cell i .

the non-singularity of the reconstruction matrix, since the CLS reconstruction corresponds to local minimization problems. For the k -exact reconstruction, the reconstruction matrix is found to be singular in certain cases [34,37]. Further analysis indicates that the iterative methods, such as the block Jacobi, Gauss–Seidel and successive over-relaxation (SOR) (with the over-relaxation factor $0 < \omega < 2$) iterations, are convergent in solving the linear equation system of the variational reconstruction.

The remainder of this paper is organized as follows. Section 2 presents the variational reconstruction in detail. Section 3 presents techniques to extend the high order FV method using the variation reconstruction to solve the two-dimensional Navier–Stokes equations, including the implementation of the boundary conditions in reconstruction, the viscous flux computation, the problem-independent shock detector and the WBAP limiter. Numerical examples are given in Section 4 to validate the performance of the proposed scheme and the concluding remarks are given in Section 5.

2. Variational reconstruction

This section presents the variational reconstruction on arbitrary unstructured meshes, i.e., the triangular, quadrilateral and mixed meshes. The computational domain Ω is partitioned into N non-overlapping control volumes, i.e., $\Omega = \cup_{i=1}^N \Omega_i$. The volume of control volume i is denoted by $\overline{\Omega}_i$. For arbitrary high order variational reconstruction, the stencil is chosen to be compact involving only the face-neighbors of the control volume of interest, and denoted by $S_i = \{\Omega_i, \Omega_{j_1}, \Omega_{j_2}, \Omega_{j_3}\}$, as shown in Fig. 1.

The reconstruction problem in the FV scheme can be stated as follows. Given the cell average

$$\bar{u}_j = \frac{1}{\overline{\Omega}_j} \iint_{\Omega_j} u(\mathbf{x}) dxdy \quad (1)$$

of a solution $u(\mathbf{x})$ on every control volume $\Omega_j \in \Omega$, a degree k polynomial

$$u_i(\mathbf{x}) = \bar{u}_i + \sum_{l=1}^{N_c(k)} u_i^l \varphi_{l,i}(\mathbf{x}) \quad (2)$$

is constructed to approximate the solution on $\Omega_i \in \Omega$, where $N_c(k)$ is the number of unknown coefficients in the polynomial, e.g., $N_c(k) = (k+1)(k+2)/2 - 1$ in two-dimensional cases. u_i^l is the unknown coefficient and $\varphi_{l,i}(\mathbf{x})$ is the zero-mean basis defined by

$$\begin{aligned} \varphi_{l,i}(\mathbf{x}) &= \delta x_i^m \delta y_i^n - \overline{\delta x_i^m \delta y_i^n}, \\ \delta x_i &= (x - x_i) / \Delta x_i, \delta y_i = (y - y_i) / \Delta y_i, \overline{\delta x_i^m \delta y_i^n} = \frac{1}{\overline{\Omega}_i} \iint_{\Omega_i} \delta x_i^m \delta y_i^n dxdy, \end{aligned} \quad (3)$$

where m and n are powers of the corresponding Taylor basis, δx_i and δy_i are the length scales for the non-dimensionalization of the basis functions to avoid growth of the condition number of the reconstruction matrix with grid refinement [32,38]. The length scales are defined following the proposal of Luo et al. [39]

$$\Delta x_i = (x_{\max} - x_{\min}) / 2, \quad \Delta y_i = (y_{\max} - y_{\min}) / 2, \quad (4)$$

where x_{\max} , y_{\max} , x_{\min} and y_{\min} are the maximum and minimum coordinates of the control volume in x - and y -direction. The following cubic reconstruction ($k=3$) polynomial using zero-mean basis is presented to illustrate the relation among the indexes l , m and n

$$\begin{aligned}
u_i(\mathbf{x}) &= \bar{u}_i + \sum_{l=1}^9 u_i^l \varphi_{l,i}(\mathbf{x}) \\
&= \bar{u}_i + u_i^1 \delta x_i + u_i^2 \delta y_i + u_i^3 (\delta x_i^2 - \overline{\delta x_i^2}) + u_i^4 (\delta x_i \delta y_i - \overline{\delta x_i \delta y_i}) + u_i^5 (\delta y_i^2 - \overline{\delta y_i^2}) \\
&\quad + u_i^6 (\delta x_i^3 - \overline{\delta x_i^3}) + u_i^7 (\delta x_i^2 \delta y_i - \overline{\delta x_i^2 \delta y_i}) + u_i^8 (\delta x_i \delta y_i^2 - \overline{\delta x_i \delta y_i^2}) + u_i^9 (\delta y_i^3 - \overline{\delta y_i^3}).
\end{aligned} \tag{5}$$

Because of the use of the zero-mean basis, the reconstruction polynomial $u_i(\mathbf{x})$ is always conservative in the sense

$$\frac{1}{|\Omega_i|} \iint_{\Omega_i} u_i(\mathbf{x}) \, dx dy = \bar{u}_i. \tag{6}$$

The variational reconstruction represents a general class of reconstruction procedures, in which the linear equation system to determine the unknown coefficients of the reconstruction polynomials is derived by minimizing the cost function using the variational method. Different cost functions result in different reconstruction procedures. In the present paper, the cost function is based on the interfacial jump integration (IJI) function, which, for a specified cell interface f , is defined by

$$I_f = \frac{1}{d_{LR}} \int_f \sum_{p=0}^k \left(\frac{1}{p!} \frac{\partial^p u_L}{\partial \tilde{x}^p} (d_{LR})^p - \frac{1}{p!} \frac{\partial^p u_R}{\partial \tilde{x}^p} (d_{LR})^p \right)^2 ds, \tag{7}$$

where L and R denote the left and right cells of the face f , d_{LR} denotes the distance between the centroids of the two cells and \tilde{x} denotes the coordinate along the normal direction. The IJI is a measure of the jump of the reconstruction polynomial and its various order of derivatives across the cell interface. The cost function is the summation of the IJI over the computational domain, i.e.,

$$I = \sum_{f=1}^{N_f} I_f, \tag{8}$$

where N_f is the number of the cell interfaces on the computational domain. The constitutive relations of the variational reconstruction are derived by minimizing the total IJI with respect to the coefficients of the reconstruction polynomial $u_i^l, l = 1, \dots, N_c(k)$ using

$$\frac{\partial I}{\partial u_i^l} = 0, \quad l = 1, \dots, N_c(k), \quad i = 1, \dots, N. \tag{9}$$

Referring to Fig. 1, the unknown coefficients u_i^l of the reconstruction polynomial on control volume Ω_i only appear in the IJI defined at the faces of Ω_i . Therefore, u_i^l is only related to the information defined on the cells belonging to stencil S_i . By substituting Eq. (2) into Eqs. (7)–(9), we obtain the following linear equations

$$\begin{aligned}
&\sum_{m=1}^{N_c(k)} \left[\sum_{j \in S_i, j \neq i} \int_{\partial \Omega_i \cap \partial \Omega_j} \sum_{p=0}^k \frac{(d_{ij})^{2p-1}}{(p!)^2} \frac{\partial^p \varphi_{l,i}}{\partial \tilde{x}^p} \frac{\partial^p \varphi_{m,i}}{\partial \tilde{x}^p} ds \right] u_i^m \\
&= \sum_{j \in S_i, j \neq i} \sum_{n=1}^{N_c(k)} \left[\int_{\partial \Omega_i \cap \partial \Omega_j} \sum_{p=0}^k \frac{(d_{ij})^{2p-1}}{(p!)^2} \frac{\partial^p \varphi_{l,i}}{\partial \tilde{x}^p} \frac{\partial^p \varphi_{n,j}}{\partial \tilde{x}^p} ds \right] u_j^n + \sum_{j \in S_i, j \neq i} \int_{\partial \Omega_i \cap \partial \Omega_j} \frac{\varphi_{l,i}}{d_{ij}} (\bar{u}_j - \bar{u}_i) ds \\
&l = 1, \dots, N_c(k), \quad i = 1, \dots, N,
\end{aligned} \tag{10}$$

which can be written in the matrix form as

$$\mathbf{A}_i \mathbf{u}_i = \sum_{j \in S_i, j \neq i} \mathbf{B}_i^j \mathbf{u}_j + \mathbf{b}_i, \quad i = 1, \dots, N, \tag{11}$$

where the matrices are

$$\begin{aligned}
\mathbf{u}_i &= [u_i^1, u_i^2, \dots, u_i^{N_c(k)}]^T, \\
\mathbf{A}_i &= \left[\sum_{j \in S_i, j \neq i} \int_{\partial\Omega_i \cap \partial\Omega_j} \sum_{p=0}^k \frac{(d_{ij})^{2p-1}}{(p!)^2} \frac{\partial^p \varphi_{l,i}}{\partial \tilde{x}^p} \frac{\partial^p \varphi_{m,i}}{\partial \tilde{x}^p} ds \right]_{N_c(k) \times N_c(k)}, \\
\mathbf{B}_i^j &= \left[\int_{\partial\Omega_i \cap \partial\Omega_j} \sum_{p=0}^k \frac{(d_{ij})^{2p-1}}{(p!)^2} \frac{\partial^p \varphi_{l,i}}{\partial \tilde{x}^p} \frac{\partial^p \varphi_{n,j}}{\partial \tilde{x}^p} ds \right]_{N_c(k) \times N_c(k)}, \\
\mathbf{b}_i &= \left[\sum_{j \in S_i, j \neq i} \int_{\partial\Omega_i \cap \partial\Omega_j} \frac{\varphi_{l,i}}{d_{ij}} (\bar{u}_j - \bar{u}_i) ds \right]_{N_c(k)}.
\end{aligned} \tag{12}$$

The face integral terms in the reconstruction matrices can be computed exactly using Gaussian quadrature formulas with sufficient precision.

The linear equation system described in Eq. (11) can be assembled into

$$\mathbf{A}\mathbf{u} = \mathbf{b}, \tag{13}$$

where

$$\mathbf{A} = \mathbf{D} - \mathbf{L} - \mathbf{U},$$

$$\mathbf{D} = \{\mathbf{A}_i\}, \mathbf{L} = \{\mathbf{B}_i^j, j < i\}, \mathbf{U} = \{\mathbf{B}_i^j, j > i\} \tag{14}$$

$$\mathbf{u} = \{\mathbf{u}_i\}, \mathbf{b} = \{\mathbf{b}_i\}.$$

The solution of Eq. (13) gives the coefficients of the reconstruction polynomials on all control volumes. Before discussing the specific solution procedures, we firstly prove that the matrix \mathbf{A} has the following properties:

- (i). \mathbf{A} is symmetric;
- (ii). \mathbf{A} is positive definite;
- (iii). $2\mathbf{D} - \mathbf{A}$ is positive definite.

Property i can be easily derived from $\mathbf{A}_i = (\mathbf{A}_i)^T$ and $\mathbf{B}_i^j = (\mathbf{B}_j^i)^T$. Property ii is proved as follows.

$$\begin{aligned}
\mathbf{u}^T \mathbf{A} \mathbf{u} &= \sum_{i=1}^N \mathbf{u}_i^T \left(\mathbf{A}_i \mathbf{u}_i - \sum_{j \in S_i, j \neq i} \mathbf{B}_i^j \mathbf{u}_j \right) \\
&= \sum_{i=1}^N \sum_{j \in S_i, j \neq i} \frac{(d_{ij})^{2p-1}}{(p!)^2} \sum_{p=0}^k \int_{\partial\Omega_i \cap \partial\Omega_j} \frac{\partial^p \hat{u}_i}{\partial \tilde{x}^p} \left(\frac{\partial^p \hat{u}_i}{\partial \tilde{x}^p} - \frac{\partial^p \hat{u}_j}{\partial \tilde{x}^p} \right) ds \\
&= \sum_{f=1}^{N_f} \int_f \sum_{p=0}^k \frac{(d_{LR})^{2p-1}}{(p!)^2} \left(\frac{\partial^p \hat{u}_L}{\partial \tilde{x}^p} - \frac{\partial^p \hat{u}_R}{\partial \tilde{x}^p} \right)^2 ds \\
&\geq 0
\end{aligned} \tag{15}$$

where $\hat{u}_i(\mathbf{x}) = \sum_{l=1}^{N_c(k)} u_l^i \varphi_{l,i}(\mathbf{x})$. If the left and right control volumes that share interface f are cell i and cell j , we have $\hat{u}_L(\mathbf{x}) = \hat{u}_i(\mathbf{x})$ and $\hat{u}_R(\mathbf{x}) = \hat{u}_j(\mathbf{x})$. It is apparent that $\hat{u}_i(\mathbf{x})$ is a zero-mean polynomial defined on each control volume satisfying

$$\int_{\Omega_i} \hat{u}_i(\mathbf{x}) dxdy = 0. \tag{16}$$

Additionally, when $\mathbf{u}^T \mathbf{A} \mathbf{u} = 0$, it can be deduced from Eq. (15) that across every cell interface f , we have

$$\frac{\partial^p \hat{u}_L}{\partial \tilde{x}^p} = \frac{\partial^p \hat{u}_R}{\partial \tilde{x}^p}, \quad p = 0, \dots, k, \tag{17}$$

or

$$\frac{\partial^p \hat{u}_i}{\partial \tilde{x}^p} = \frac{\partial^p \hat{u}_j}{\partial \tilde{x}^p}, \quad p = 0, \dots, k. \quad (18)$$

It is straightforward to prove that Eq. (18) leads to $\hat{u}_i(\mathbf{x}) = \hat{u}_j(\mathbf{x})$. Repeating this analysis on every cell interface, we conclude that for all i , $\hat{u}_i(\mathbf{x})$ are degenerated into a single degree k polynomial $\hat{u}(\mathbf{x}) = \sum_{l=1}^{N_c(k)} u^l \varphi_l(\mathbf{x})$ satisfying

$$\int_{\Omega_i} \hat{u}(\mathbf{x}) \, dx dy = 0, \quad i = 1, \dots, N. \quad (19)$$

If there are sufficient number of cells in the computational domain and the grid is well positioned (not all elements are aligned on a straight line), Eq. (19) implies

$$\hat{u}(\mathbf{x}) = 0, \quad (20)$$

or

$$u_i^l = 0, \quad (21)$$

for any i, l . This proves that $\mathbf{u}^T \mathbf{A} \mathbf{u} = 0$ if and only if $\mathbf{u} = 0$. Therefore, \mathbf{A} is positive definite. Property iii can be proved in a similar way.

According to property i and property ii, matrix of the linear equation system of the variational reconstruction is symmetric and positive definite. Therefore, the matrix is invertible, i.e., there exists a unique solution to the reconstruction problem. This is a significant advantage over both the CLS and k -exact reconstructions, since the reconstruction matrix of neither the CLS nor the k -exact reconstruction can be guaranteed to be non-singular.

The solution of Eq. (13) relies on all control volumes in the computational domain. If a direct solver is used to solve Eq. (13), the solution procedure is by no means compact. Therefore, in the present paper, we are interested in the iterative solvers that can maintain the compactness of the solution procedure. It should be noticed that the “compactness” used in the present paper is always in the sense that the solution procedure is “operationally” compact. The exact meaning is that in any single operation, we only use the information of current and face-neighboring cells. As a consequence, we only need to maintain the data structures defined in terms of a compact stencil. This property is sufficient to ease the data transfer between different sub-domains in the parallel computing based on the domain decomposition approach and is also beneficial to reduce the cache missing encountered by traditional high order FV schemes using a very large stencil. There are several iterative solvers that can keep compactness of the solution procedure when solving Eq. (13), such as the block Jacobi method

$$\mathbf{u}_i^{(s+1)} = \sum_{j \in S_i, j \neq i} [(\mathbf{A}_i)^{-1} \mathbf{B}_i^j] \mathbf{u}_j^{(s)} + (\mathbf{A}_i)^{-1} \mathbf{b}_i, \quad i = 1, \dots, N, \quad (22)$$

the block Gauss–Seidel method

$$\mathbf{u}_i^{(s+1)} = \sum_{j \in S_i, j < i} [(\mathbf{A}_i)^{-1} \mathbf{B}_i^j] \mathbf{u}_j^{(s+1)} + \sum_{j \in S_i, j > i} [(\mathbf{A}_i)^{-1} \mathbf{B}_i^j] \mathbf{u}_j^{(s)} + (\mathbf{A}_i)^{-1} \mathbf{b}_i, \quad i = 1, \dots, N, \quad (23)$$

and the block SOR method

$$\mathbf{u}_i^{(s+1)} = (1 - \omega) \mathbf{u}_i^{(s)} + \omega \left\{ \sum_{j \in S_i, j < i} [(\mathbf{A}_i)^{-1} \mathbf{B}_i^j] \mathbf{u}_j^{(s+1)} + \sum_{j \in S_i, j > i} [(\mathbf{A}_i)^{-1} \mathbf{B}_i^j] \mathbf{u}_j^{(s)} + (\mathbf{A}_i)^{-1} \mathbf{b}_i \right\}, \quad i = 1, \dots, N, \quad (24)$$

where s denotes the iteration step. Furthermore, according to numerical analysis theory [40], the block Gauss–Seidel and block SOR ($0 < \omega < 2$) methods are convergent if matrix \mathbf{A} has property i and property ii. The block Jacobi method converges if matrix \mathbf{A} has properties i–iii.

The condition numbers and spectral radii of the block Jacobi (ρ_J), block Gauss–Seidel (ρ_{GS}) and block SOR (ρ_{SOR}) iteration methods for the linear equation system of the variational reconstruction on the meshes shown in Fig. 4 are listed in Table 1. The results in Table 1 show that the block SOR method with ω around 1.3 has the smallest spectral radius, i.e., the fastest speed of convergence. Therefore, in this paper, the iterative solver for the variational reconstruction is the block SOR method using an over-relaxation factor $\omega = 1.3$.

If an iterative solver discussed above is used to solve Eq. (13) to complete convergence, the computational cost is still very large. Fortunately, in [2], we have proposed the so-called reconstruction and time integration coupled iteration method which can achieve very high efficiency in the overall solution procedure. This approach can be readily used in the case of the variational reconstruction. The feasibility of this approach is based on the following observations. The first case is

Table 1

Condition number of the linear equation system of the variational reconstruction and spectral radii of the Jacobi, Gauss–Seidel and SOR methods on the four meshes shown in Fig. 4.

Mesh	Regular triangular	Irregular triangular	Regular quadrilateral	Irregular quadrilateral
Condition number	94.4513	30548.6	265.909	1115.33
ρ_J	0.851996	0.943152	0.787827	0.82605
ρ_{GS}	0.716773	0.889529	0.629014	0.683894
$\rho_{SOR}, \omega = 1.1$	0.652158	0.864762	0.549735	0.612841
$\rho_{SOR}, \omega = 1.2$	0.561715	0.832882	0.444236	0.514222
$\rho_{SOR}, \omega = 1.3$	0.376548	0.789234	0.456616	0.434722
$\rho_{SOR}, \omega = 1.4$	0.454413	0.721679	0.542257	0.512903

the steady-state simulation in terms of the time-dependent equations in which the temporal accuracy will not affect the converged steady-state solutions. Therefore, the iterative solver of the variational reconstruction needs not to reach full convergence, and can be implemented only once in a single time step. The coupling between the reconstruction and the temporal discretization scheme makes the two procedures achieve their convergence synchronously. The second case is the unsteady simulation using the dual time stepping technique [41,42] which can be considered as solving a modified steady problem by advancing in pseudo time at each physical time step. Similar to the steady-state simulation, the iteration in the reconstruction can be also performed only once in every pseudo time step.

The time integration scheme for steady-state simulation is the matrix-free GMRES+LU-SGS method [43]. The time integration scheme for unsteady-state simulation is the three-stage, fourth-order accurate singly-diagonally implicit Runge–Kutta (SDIRK) method [44], in which the solver for the inner iteration is the matrix-free LU-SGS approach. In practice, on each control volume, the variational reconstruction is implemented by simply solving Eq. (24) once in a time step for steady flow simulation or in the inner iteration of a dual time stepping scheme for unsteady flow simulation. This procedure involves only the information on the compact stencil S_i shown in Fig. 1. In terms of the computational cost, Eq. (24) is very close to the traditional k -exact reconstruction of the same order. Therefore, by using the coupled iteration method, the implicit property of the variational or CLS reconstruction does not lead to any extra computational cost. The interested readers are encouraged to refer [2] for further details. In [2], the algorithm of the reconstruction and time integration coupled iteration method was also presented. This algorithm can be also applied to the numerical scheme of the present paper.

After the introduction of the variational reconstruction procedure, several remarks are in order.

Remark 1. To further improve the variational reconstruction and demonstrate that the present approach is superior to the CLS reconstruction proposed in our previous papers [1,2], the one-dimensional case is discussed in this remark. On the uniform grid with grid size h , the one-dimensional IJI of the cubic variational reconstruction is defined as

$$I_f = (u_L - u_R)^2 + h^2 \left(\frac{\partial u_L}{\partial x} - \frac{\partial u_R}{\partial x} \right)^2 + \frac{h^4}{4} \left(\frac{\partial^2 u_L}{\partial x^2} - \frac{\partial^2 u_R}{\partial x^2} \right)^2 + \frac{h^6}{36} \left(\frac{\partial^3 u_L}{\partial x^3} - \frac{\partial^3 u_R}{\partial x^3} \right)^2. \quad (25)$$

In [1], weight functions are introduced into the one-dimensional CLS reconstruction schemes to achieve the optimal spectral properties. Following this idea, a simple weight function is introduced into the IJI and the IJI is redefined as

$$I_f = w^2 (u_L - u_R)^2 + w^2 h^2 \left(\frac{\partial u_L}{\partial x} - \frac{\partial u_R}{\partial x} \right)^2 + \frac{h^4}{4} \left(\frac{\partial^2 u_L}{\partial x^2} - \frac{\partial^2 u_R}{\partial x^2} \right)^2 + \frac{h^6}{36} \left(\frac{\partial^3 u_L}{\partial x^3} - \frac{\partial^3 u_R}{\partial x^3} \right)^2, \quad (26)$$

where w is the only free parameter in the scheme. The Fourier analysis shows that the optimal value of w is positive infinity, which can be explained by that a larger w increases the relative importance of the jumps of u and $\frac{\partial u}{\partial x}$ in the cost function and generates piece-wise reconstruction polynomials with smaller jumps of u and $\frac{\partial u}{\partial x}$. The decrease of the jump of u reduces the dissipation and the decrease of the jump of $\frac{\partial u}{\partial x}$ improves the accuracy of viscous flux computation and is observed to be able to decrease the dispersion error. However, a scheme with very large w has very small dissipation and is not robust. In practice, the fourth-order variational reconstruction with $w = 5$ is found to achieve the balance of accuracy and robustness and is therefore considered to be optimal. The dispersion and dissipation properties of the optimal fourth-order variational and CLS reconstructions are shown in Fig. 2. The spectral properties of the sixth-order central difference scheme (C6) and the sixth-order tridiagonal scheme (T6) proposed in [45] are also shown in Fig. 2 for the purpose of comparison. The comparison shows that the spectral behavior of the variational reconstruction is very close to the T6 scheme and is much better than the CLS reconstruction. The von Neumann stability analysis in one-dimensional case is also performed for the fourth-order variational reconstruction in conjunction with the three-stage TVD Runge–Kutta scheme [46]. The relations between the amplification factor and the wavenumber at CFL number $c = 1$ for the fourth-order variational and CLS reconstructions are depicted in Fig. 3. According to Fig. 3, both reconstruction schemes are stable.

Remark 2. The boundary treatment of the variational reconstruction is more accurate and flexible than the CLS reconstruction. In the variational reconstruction, there is no need to reduce the degrees of reconstruction polynomials at boundary

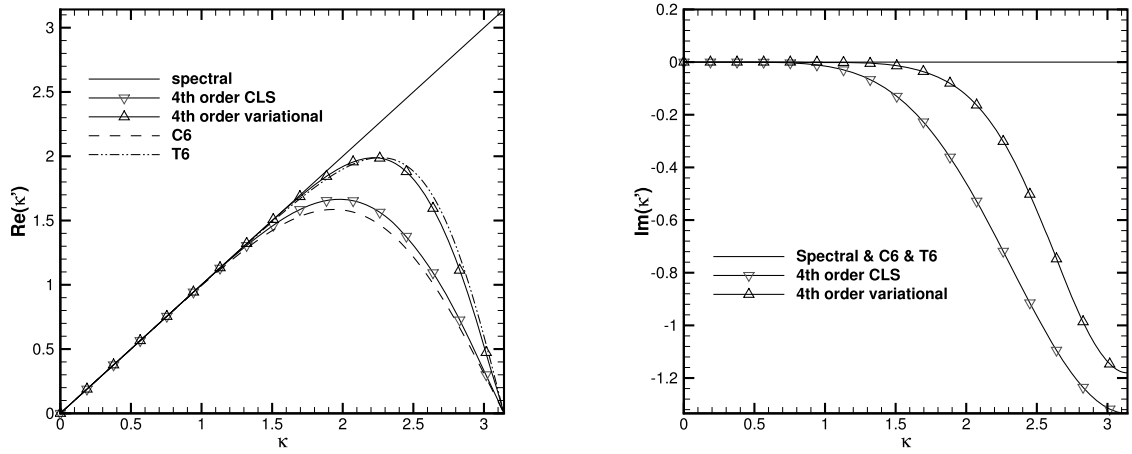


Fig. 2. Dispersion and dissipation properties of the fourth-order variational and CLS reconstructions.

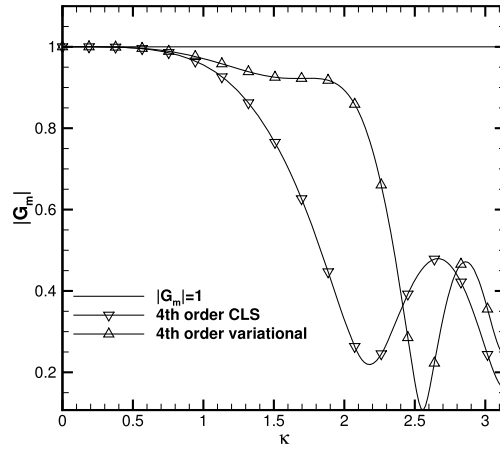


Fig. 3. Amplification factors for the fourth-order variational and CLS reconstruction schemes using TVD RK3. The CFL number is 1.0.

cells. While in multi-dimensional CLS reconstruction, the reconstruction polynomial at boundary cells must be one-order lower in accuracy than that at inner cells because there are not enough constitutive equations to obtain a stable reconstruction scheme without the decrease of accuracy at the boundary cells. Therefore, the variational reconstruction can achieve higher order of accuracy than the CLS reconstruction in simulation of problems with physical boundaries. Furthermore, various boundary conditions can be implemented straightforwardly by specifying proper IJI at the boundary. Details of the implementation of the non-slip solid wall and the symmetry boundary conditions are presented in Section 3.1.

Remark 3. The variational reconstruction is a general framework to reconstruct piecewise polynomials on unstructured grids. Besides the IJI proposed in this Section, various definitions of the jump integration in Eq. (7) can be used in the variational reconstruction. For example, the jump integration can be defined as

$$\begin{aligned}
 I_f = & \frac{1}{d_{LR}} \int_L \sum_{p=0}^k \left(\frac{1}{p!} \frac{\partial^p u_L}{\partial \tilde{x}^p} (d_{LR})^p - \frac{1}{p!} \frac{\partial^p u_R}{\partial \tilde{x}^p} (d_{LR})^p \right)^2 dx dy \\
 & + \frac{1}{d_{LR}} \int_R \sum_{p=0}^k \left(\frac{1}{p!} \frac{\partial^p u_L}{\partial \tilde{x}^p} (d_{LR})^p - \frac{1}{p!} \frac{\partial^p u_R}{\partial \tilde{x}^p} (d_{LR})^p \right)^2 dx dy,
 \end{aligned} \tag{27}$$

or

$$\begin{aligned}
I_f = & \frac{1}{d_{LR}} \sum_{p=0}^k \sum_{m=0}^p \frac{(d_{LR})^{2p}}{(p!)^2} \left(\frac{1}{\bar{\Omega}_L} \int_{\Omega_L} \frac{\partial^p u_L}{\partial x^m \partial y^{p-m}} dx dy - \frac{1}{\bar{\Omega}_L} \int_{\Omega_L} \frac{\partial^p u_R}{\partial x^m \partial y^{p-m}} dx dy \right)^2 \\
& + \frac{1}{d_{LR}} \sum_{p=0}^k \sum_{m=0}^p \frac{(d_{LR})^{2p}}{(p!)^2} \left(\frac{1}{\bar{\Omega}_R} \int_{\Omega_R} \frac{\partial^p u_L}{\partial x^m \partial y^{p-m}} dx dy - \frac{1}{\bar{\Omega}_R} \int_{\Omega_R} \frac{\partial^p u_R}{\partial x^m \partial y^{p-m}} dx dy \right)^2.
\end{aligned} \tag{28}$$

It is noticed that these jump integrations are defined on the control volumes instead of the cell interfaces. Preliminary tests show that all these approaches can obtain stable high order FV schemes on unstructured grids. This raises an interesting problem about what are the general requirements for designing the jump integrations. Two apparent constraints for designing the jump integrations are that the resulting reconstruction polynomials should be k -exact and relying on compact stencils, which are satisfied by all the proposed jump integrations in this section.

Remark 4. We notice that the implicit nature of the variational reconstruction does not result in non-sparse Jacobian matrix in implicit time integration procedures, such as the LU-SGS smoother. In fact, the implicit time integration algorithm of the present paper is identical to that of the traditional second order FV schemes on unstructured grids. Unlike the implicit schemes for DG methods [47–49], the exact or high-order approximate Jacobian matrix is not needed. Instead, we use the first order approximation in the linearization of the residual by assuming the time increments of the dependent variables are piece-wise constant. Therefore, only the face-neighbors are involved in updating the solution of the control volume of interest, which means that the effective Jacobian matrix is sparse.

3. Extension to Navier–Stokes equations

In this paper, the compact high order finite volume method is applied to two-dimensional compressible viscous flow simulations on arbitrary unstructured grids. The governing equations are the two-dimensional Navier–Stokes equations

$$\frac{\partial \mathbf{U}}{\partial t} + \nabla \cdot [\mathbf{F}_i(\mathbf{U}) - \mathbf{F}_v(\mathbf{U}, \nabla \mathbf{U})] = 0, \tag{29}$$

where the conservative variables \mathbf{U} and Cartesian components $f_i(\mathbf{U})$ and $g_i(\mathbf{U})$ of the inviscid flux vectors \mathbf{F}_i are

$$\mathbf{U} = \begin{pmatrix} \rho \\ \rho u \\ \rho v \\ E \end{pmatrix}, \quad f_i(\mathbf{U}) = \begin{pmatrix} \rho u \\ \rho u^2 + p \\ \rho uv \\ u(E + p) \end{pmatrix}, \quad g_i(\mathbf{U}) = \begin{pmatrix} \rho v \\ \rho uv \\ \rho v^2 + p \\ v(E + p) \end{pmatrix}, \tag{30}$$

and Cartesian components $f_v(\mathbf{U}, \nabla \mathbf{U})$ and $g_v(\mathbf{U}, \nabla \mathbf{U})$ of the viscous flux vectors \mathbf{F}_v are

$$\begin{aligned}
f_v(\mathbf{U}, \nabla \mathbf{U}) &= \left(0, \tau_{xx}, \tau_{xy}, u\tau_{xx} + v\tau_{xy} + \kappa \frac{\partial T}{\partial x} \right)^T, \\
g_v(\mathbf{U}, \nabla \mathbf{U}) &= \left(0, \tau_{xy}, \tau_{yy}, u\tau_{xy} + v\tau_{yy} + \kappa \frac{\partial T}{\partial y} \right)^T,
\end{aligned} \tag{31}$$

with the viscous stress computed by

$$\begin{aligned}
\tau_{xx} &= 2\mu \frac{\partial u}{\partial x} + \lambda \mu \left(\frac{\partial u}{\partial x} + \frac{\partial v}{\partial y} \right), \\
\tau_{xy} &= \mu \left(\frac{\partial v}{\partial x} + \frac{\partial u}{\partial y} \right), \\
\tau_{yy} &= 2\mu \frac{\partial v}{\partial y} + \lambda \mu \left(\frac{\partial u}{\partial x} + \frac{\partial v}{\partial y} \right).
\end{aligned} \tag{32}$$

In the above equations, ρ denotes the density, $(u, v)^T$ is the velocity vector, μ is the dynamic viscosity, T is the temperature, p is the pressure and E is the total energy defined by

$$E = \frac{p}{\gamma - 1} + \frac{1}{2} \rho (u^2 + v^2), \tag{33}$$

with a constant ratio of specific heat $\gamma = 1.4$. According to the Stokes hypothesis, $\lambda = -2/3$. The heat conductivity is computed by $\kappa = C_p \mu / Pr$, where C_p is the specific heat at constant pressure and Pr is the Prandtl number. The temperature is computed by the following equation of state

$$T = \frac{\gamma p}{(\gamma - 1) C_p \rho}. \quad (34)$$

The reconstruction procedure presented in Section 2 can be readily extended to the FV scheme solving the Navier–Stokes equations by applying the reconstruction technique to each component of the conservative variables. We reconstruct the conservative variables rather than the primitive or characteristic variables, because for FV schemes, only the cell-averages of the conservative variables are available while the cell-averages of the primitive and characteristic variables need to be decoded from the cell-averages of the conservative variables. The transformation of cell-averages from conservative to primitive variables are only second-order accurate. The reconstruction in characteristic space is not suitable for FV schemes on unstructured grids because there is not a certain characteristic direction for the entire domain. To suppress non-physical oscillations near discontinuities, a problem-independent shock detector [50] and the WBAP limiter [51,52] are used in supersonic and transonic flow simulations. The limiting procedure used in this paper is the successive limiting procedure based on the characteristic variables. Implementation details of the shock detector and the limiter will be presented in Section 3.3. After the reconstruction and limiting procedures, the inviscid flux is computed using a proper Riemann solver. The Riemann solver used in the present paper is the Roe–Pike approximate Riemann solver [53,54] with the entropy correction of Sanders et al. [55]. The viscous flux computation procedure will be presented in Section 3.2. The cell-averages of the conservative variables could be updated via the implicit time integration scheme presented in Section 2 after the computation of the numerical fluxes.

To complete the solution procedure for the Navier–Stokes equations, the implementation of the boundary conditions, the computation of the viscous flux, the shock detector and the WBAP limiter are presented in the following three subsections.

3.1. Implementation of boundary conditions in reconstruction

To ensure the accuracy of reconstructions up to the boundary, the effects of the boundary conditions (BCs) need to be considered in the reconstruction procedure. Implementation of the BCs is complicated for the k -exact and the CLS reconstructions. For example, to implement the non-slip solid wall BC in the k -exact and the CLS reconstructions, the constrained least-squares problem needs to be solved [31].

On the other hand, in the variational construction, the effect of BCs can be modeled straightforwardly by the introduction of proper boundary IJl so that the cost function is given by

$$I = \sum_{f=1}^{N_f} I_f + \sum_{bf=1}^{N_{bf}} I_{bf}, \quad (35)$$

where N_{bf} is the number of the boundary faces.

For the non-slip wall BC, the boundary IJl term for the reconstruction of a conservative variable q is defined as

$$I_{bf} = \frac{1}{d_{bf}} \int_{bf} (q_L - q_{bf})^2 ds, \quad (36)$$

where L denotes the cell adjacent to the boundary face bf , d_{bf} is the distance between the centroid of cell L and the midpoint of bf and q_{bf} is the boundary value of q . For example, for the stationary non-slip and isothermal solid wall BC with wall temperature T_{wall} , the boundary values of conservative variables are given as [56]

$$\begin{aligned} \rho_{bf} &= \rho_L, \quad E_{bf} = \frac{C_p \rho_L T_{wall}}{\gamma}, \\ (\rho u)_{bf} &= -(\rho u)_L, \quad (\rho v)_{bf} = -(\rho v)_L. \end{aligned} \quad (37)$$

For the symmetry BC, the boundary IJl term for the reconstruction of a conservative variable q is defined as

$$I_{bf} = \frac{1}{d_{bf}} \int_{bf} \sum_{p=0}^k \left(\frac{1}{p!} \frac{\partial^p q_L}{\partial \tilde{x}^p} (d_{bf})^p - \frac{1}{p!} \frac{\partial^p q_{bf}}{\partial \tilde{x}^p} (d_{bf})^p \right)^2 ds. \quad (38)$$

The boundary values of conservative variables ρ and E are given as

$$\begin{aligned} q_{bf} &= q_L, \\ \frac{\partial q_{bf}}{\partial \tilde{x}} &= -\frac{\partial q_L}{\partial \tilde{x}}, \quad \frac{\partial^2 q_{bf}}{\partial \tilde{x}^2} = \frac{\partial^2 q_L}{\partial \tilde{x}^2}, \quad \frac{\partial^3 q_{bf}}{\partial \tilde{x}^3} = -\frac{\partial^3 q_L}{\partial \tilde{x}^3}. \end{aligned} \quad (39)$$

The boundary values of conservative variables ρu and ρv are determined by the following equations

$$\begin{aligned}
(\rho u, \rho v)_{bf} \cdot \mathbf{n} &= -(\rho u, \rho v)_L \cdot \mathbf{n}, \quad (\rho u, \rho v)_{bf} \cdot \mathbf{t} = (\rho u, \rho v)_L \cdot \mathbf{t}, \\
\left(\frac{\partial \rho u}{\partial \tilde{x}}, \frac{\partial \rho v}{\partial \tilde{x}} \right)_{bf} \cdot \mathbf{n} &= \left(\frac{\partial \rho u}{\partial \tilde{x}}, \frac{\partial \rho v}{\partial \tilde{x}} \right)_L \cdot \mathbf{n}, \quad \left(\frac{\partial \rho u}{\partial \tilde{x}}, \frac{\partial \rho v}{\partial \tilde{x}} \right)_{bf} \cdot \mathbf{t} = - \left(\frac{\partial \rho u}{\partial \tilde{x}}, \frac{\partial \rho v}{\partial \tilde{x}} \right)_L \cdot \mathbf{t}, \\
\left(\frac{\partial^2 \rho u}{\partial \tilde{x}^2}, \frac{\partial^2 \rho v}{\partial \tilde{x}^2} \right)_{bf} \cdot \mathbf{n} &= - \left(\frac{\partial^2 \rho u}{\partial \tilde{x}^2}, \frac{\partial^2 \rho v}{\partial \tilde{x}^2} \right)_L \cdot \mathbf{n}, \quad \left(\frac{\partial^2 \rho u}{\partial \tilde{x}^2}, \frac{\partial^2 \rho v}{\partial \tilde{x}^2} \right)_{bf} \cdot \mathbf{t} = \left(\frac{\partial^2 \rho u}{\partial \tilde{x}^2}, \frac{\partial^2 \rho v}{\partial \tilde{x}^2} \right)_L \cdot \mathbf{t}, \\
\left(\frac{\partial^3 \rho u}{\partial \tilde{x}^3}, \frac{\partial^3 \rho v}{\partial \tilde{x}^3} \right)_{bf} \cdot \mathbf{n} &= \left(\frac{\partial^3 \rho u}{\partial \tilde{x}^3}, \frac{\partial^3 \rho v}{\partial \tilde{x}^3} \right)_L \cdot \mathbf{n}, \quad \left(\frac{\partial^3 \rho u}{\partial \tilde{x}^3}, \frac{\partial^3 \rho v}{\partial \tilde{x}^3} \right)_{bf} \cdot \mathbf{t} = - \left(\frac{\partial^3 \rho u}{\partial \tilde{x}^3}, \frac{\partial^3 \rho v}{\partial \tilde{x}^3} \right)_L \cdot \mathbf{t},
\end{aligned} \tag{40}$$

where $\mathbf{n} = (n_x, n_y)^T$ is the unit outward normal vector of face bf , $\mathbf{t} = (-n_y, n_x)^T$ is the unit tangential vector of face bf .

3.2. Viscous flux computation

This subsection presents a simple and efficient procedure to compute the viscous flux using the piece-wise polynomial distributions of the conservative variables obtained by the reconstruction. For a specified cell interface f , we are to compute the viscous flux on the cell interface using the reconstruction polynomial \mathbf{U}_L of the left cell L and the reconstruction polynomial \mathbf{U}_R of the right cell R . The viscous flux computation procedure consists of the following three steps.

Step 1. Compute the “averaged” gradients of the conservative variables based on the solution of linear diffusive generalized Riemann problem (dGRP) [57] in normal direction as follows

$$\begin{aligned}
\frac{\partial \mathbf{U}}{\partial x} &= \frac{1}{2} \left(\frac{\partial \mathbf{U}_L}{\partial x} + \frac{\partial \mathbf{U}_R}{\partial x} \right) + \frac{1}{2\Delta\tilde{x}} (\mathbf{U}_R - \mathbf{U}_L) n_x, \\
\frac{\partial \mathbf{U}}{\partial y} &= \frac{1}{2} \left(\frac{\partial \mathbf{U}_L}{\partial y} + \frac{\partial \mathbf{U}_R}{\partial y} \right) + \frac{1}{2\Delta\tilde{x}} (\mathbf{U}_R - \mathbf{U}_L) n_y,
\end{aligned} \tag{41}$$

where $(n_x, n_y)^T$ is the unit normal vector pointing to cell R and the characteristic length scale $\Delta\tilde{x}$ of the cell interface f is chosen, according to Hartmann et al. [58], as

$$\Delta\tilde{x} = \frac{\min(\overline{\Omega}_L, \overline{\Omega}_R)}{\overline{S}_f}, \tag{42}$$

where \overline{S}_f is the length of the cell interface f .

Step 2. Compute gradients of the primitive variables using the gradients of the conservative variables obtained by step 1 via the following partial differential operations

$$\begin{aligned}
\nabla u &= \frac{1}{\tilde{\rho}^2} [\tilde{\rho} \nabla(\rho u) - \tilde{\rho} \tilde{u} \nabla \rho], \\
\nabla v &= \frac{1}{\tilde{\rho}^2} [\tilde{\rho} \nabla(\rho v) - \tilde{\rho} \tilde{v} \nabla \rho], \\
\nabla p &= (\gamma - 1) \left\{ \nabla E - \frac{1}{2} [\tilde{u} \nabla(\rho u) + \tilde{\rho} \tilde{u} \nabla u + \tilde{v} \nabla(\rho v) + \tilde{\rho} \tilde{v} \nabla v] \right\}, \\
\nabla T &= \frac{\gamma}{(\gamma - 1) C_p \tilde{\rho}^2} [\tilde{\rho} \nabla p - \tilde{p} \nabla \rho],
\end{aligned} \tag{43}$$

where the average state of a primitive variable q is computed by $\tilde{q} = (q_L + q_R)/2$.

Step 3. Compute the viscous flux using the gradients and the average states of the primitive variables obtained by step 2.

The dGRP-flux scheme, which is used to compute diffusive flux on cell interfaces using piece-wise high-order polynomial distribution, was originally proposed for both FV and DG methods solving one-dimensional diffusion problems [57]. It was later extended to multi-dimensional DG schemes for Navier–Stokes equations by Gassner et al. [59]. In the present paper, Eq. (41) is the diffusive flux formulation designed for the FV method based on dGRP [57]. In the FV method, the penalty terms in Eq. (41) are used to suppress possible odd-even decoupling modes in the numerical solutions. The removal of the penalty terms does not affect the consistency of the numerical schemes, while the DG methods are inconsistent without these terms. Similar approaches have already been used in cell-centered FV schemes [60,61].

3.3. The problem-independent shock detector and the WBAP limiter

This subsection presents the problem-independent shock detector and the WBAP limiter. The shock detector, which is used to identify trouble cells, relies on the smoothness indicator IS_i defined by [50]

$$IS_i = \frac{\sum_{j \in S_i, j \neq i} |u_i(\mathbf{x}_i) - u_j(\mathbf{x}_i)|}{N_j h_i^{(k+1)/2} \max\{\bar{u}_j | j \in S_i\}}, \quad (44)$$

where N_j stands for the number of face-neighboring cells, i.e., $N_j = 3$ for triangular cell and $N_j = 4$ for quadrilateral cell. The following condition is used to distinguish the smooth region from the region near discontinuities

$$u_i(\mathbf{x}_i) - u_j(\mathbf{x}_i) = \begin{cases} O(h_i^{k+1}), & \text{in smooth region} \\ O(1), & \text{near discontinuity} \end{cases} \quad (45)$$

Therefore, as the cell size $h_i \rightarrow 0$, $IS_i \rightarrow 0$ is in smooth regions and $IS_i \rightarrow \infty$ is near the discontinuities. The shock detector is defined by

$$(IS_i < \bar{S}_{dis}) = \begin{cases} \text{true}, & \text{smooth region} \\ \text{false}, & \text{shock region} \end{cases} \quad (46)$$

Generally, $\bar{S}_{dis} = 3$ is chosen for the fourth-order FV scheme, and $\bar{S}_{dis} = 1$ for the third and second-order FV schemes. These parameters work well for test cases with discontinuities of the present paper and are problem-independent.

The WBAP limiter [51,52] is used to suppress non-physical oscillations on the trouble cells. Similar to the limiting procedure of the WENO schemes, on one control volume, several candidate reconstruction polynomials need to be provided. The construction of candidate polynomials for the WBAP limiter are obtained through the so-called secondary reconstruction (SR) technique. The piece-wise reconstruction polynomials obtained by the variational reconstruction procedure presented in Section 2 is called the primary reconstruction polynomials. The SR uses the continuations of the primary reconstruction polynomials on face-neighbors of the current cell as the additional candidate polynomials. For example, the three SRs of the cell i shown in Fig. 1 are

$$u_{j \rightarrow i}(\mathbf{x}) = \bar{u}_i + \sum_{l=1}^{N_c(k)} u_{j \rightarrow i}^l \varphi_{l,i}(\mathbf{x}), \quad j = j_1, j_2, j_3. \quad (47)$$

Detailed formulations of the SR are presented in [1,52].

In the WBAP limiter, the limited reconstruction polynomial $\tilde{u}_i(\mathbf{x})$ is computed by a non-linear average of $u_i(\mathbf{x})$ and $u_{j \rightarrow i}(\mathbf{x})$ in the form

$$\begin{aligned} \tilde{u}_i(\mathbf{x}) &= \bar{u}_i + \sum_{l=1}^{N_c(k)} \tilde{u}_i^l \varphi_{l,i}(\mathbf{x}), \\ \tilde{u}_i^l &= L(u_i^l, u_{j_1 \rightarrow i}^l, u_{j_2 \rightarrow i}^l, u_{j_3 \rightarrow i}^l), \end{aligned} \quad (48)$$

where

$$L(a_0, a_1, a_2, \dots, a_J) = a_0 \cdot W(1, \frac{a_1}{a_0}, \frac{a_2}{a_0}, \dots, \frac{a_J}{a_0}). \quad (49)$$

W is the WBAP limiting function. In this paper, we use the WBAP-L2 limiting function [51]

$$W = W^{L2}(1, \theta_1, \dots, \theta_J) = \frac{n_p + \sum_{m=1}^J 1/\theta_m^{p-1}}{n_p + \sum_{m=1}^J 1/\theta_m^p}, \quad (50)$$

where $n_p = 10$ and $p = 4$.

The WBAP limiter is applied in a successive manner in terms of the characteristic variables. The key ingredient of the successive limiting procedure is to apply the limiter to high order derivatives first over the entire domain and the lower order derivatives of the SRs are evaluated in terms of the already limited high order derivatives. This approach yields a very robust limiting procedure. Implementation details of the successive limiting procedure in characteristic space are presented in [1,62].

4. Numerical results

The fourth-order VFV scheme is applied to solve a number of two-dimensional benchmark test cases to assess accuracy, efficiency and shock capturing capability of the scheme. In the simulations of some test cases, the accuracy of the scheme

Table 2

Accuracy test results for the manufactured Navier–Stokes solution problem on triangular meshes.

Grid size	Schemes	L_2 error	Order	L_2 error	Order
		Regular		Irregular	
1/10	2nd order FV	5.08E–03		1.43E–02	
1/20		1.11E–03	2.20	3.16E–03	2.18
1/40		2.96E–04	1.90	7.08E–04	2.16
1/80		7.75E–05	1.93	1.79E–04	1.99
1/10	4th order CLSFV	4.05E–04		1.94E–03	
1/20		1.59E–05	4.67	9.72E–05	4.32
1/40		1.04E–06	3.93	5.10E–06	4.25
1/80		6.89E–08	3.92	3.39E–07	3.91
1/10	4th order VFV	3.55E–04		1.00E–03	
1/20		1.30E–05	4.77	4.71E–05	4.41
1/40		7.54E–07	4.10	2.84E–06	4.05
1/80		4.36E–08	4.11	1.86E–07	3.93

is measured in terms the errors of the numerical solutions in L_1 , L_2 and L_∞ norms which are defined according to Wang et al. [63]. For example, the L_2 error of density is defined as

$$Error_{L_2(\Omega)} = \left[\frac{\sum_{i=1}^N (\bar{\rho}_i - \bar{\rho}_i^{exact})^2 \bar{\Omega}_i}{\sum_{i=1}^N \bar{\Omega}_i} \right]^{1/2}. \quad (51)$$

4.1. Manufactured solution for Navier–Stokes equations

A manufactured solution is solved using the VFV scheme to test its accuracy and efficiency in solving two-dimensional Navier–Stokes equations. The manufactured solution is chosen as

$$\begin{pmatrix} \rho \\ u \\ v \\ T \end{pmatrix} = \begin{pmatrix} 1 + A_\rho \sin(\omega t - k_x x - k_y y) \\ 1 + A_v \cos(\omega t - k_x x - k_y y) \\ 1 + A_v \cos(\omega t - k_x x - k_y y) \\ 1 + A_t \sin(\omega t - k_x x - k_y y) \end{pmatrix}, \quad (52)$$

where $A_\rho = A_v = 0.25$, $A_t = 0.1$, and $\omega = k_x = k_y = 2\pi$. The pressure is computed by the equation of state as follows

$$p = \frac{\gamma - 1}{\gamma} C_p \rho T \quad (53)$$

where $C_p = 3.5$. The dynamic viscosity is $\mu = 0.01$ and the Prandtl number is $Pr = 1$. The source term \mathbf{S} that is added to the right-hand side of Eq. (29) to balance the left-hand side can then be analytically derived. The expressions of \mathbf{S} are rather complex and thus are omitted.

The computational domain is $[0, 1] \times [0, 1]$. Translational periodic boundary conditions are imposed for the left/right and top/bottom boundaries respectively. The computations are performed for a time period $t = 1$. Four types of successively refined meshes, namely the regular triangular, irregular triangular, regular quadrilateral and irregular quadrilateral meshes, are used in the computations and shown in Fig. 4.

The grid sizes are chosen to be 1/10 to 1/80, and the corresponding physical time steps are 1/60 to 1/480 for the regular triangular meshes, 1/80 to 1/640 for the irregular triangular meshes and 1/20 to 1/160 for both regular and irregular quadrilateral meshes. The CFL number for the local pseudo time step is 1000 and the convergence criterion for the inner iteration is that the residual decreases by 7 orders of magnitude. The accuracy tests of the second-order k -exact and the fourth-order CLS FV schemes are also performed for the purpose of comparison.

The errors of density in terms of L_2 norms and the rates of convergence are listed in Table 2 and Table 3. The results in Table 2 and Table 3 show that all the schemes achieve the desired high order accuracy and the fourth-order VFV scheme is more accurate than the fourth-order CLSFV scheme. Furthermore, the two fourth-order FV schemes are remarkably more accurate than the second-order FV scheme.

The efficiency comparison is shown in Fig. 5. Fig. 5 shows that the fourth-order VFV scheme can achieve the same accuracy using less CPU time than the CLSFV scheme on relatively high accuracy level, which means that the VFV scheme is more efficient than the CLSFV scheme. Furthermore, both the fourth-order schemes are remarkably efficient than the second-order scheme. For example, on the regular triangular meshes, the second-order scheme needs to spend about 70 times more CPU time than the fourth-order schemes to achieve accuracy level of 1.0E–04, that demonstrates the advantage of the high order methods over the second-order methods.

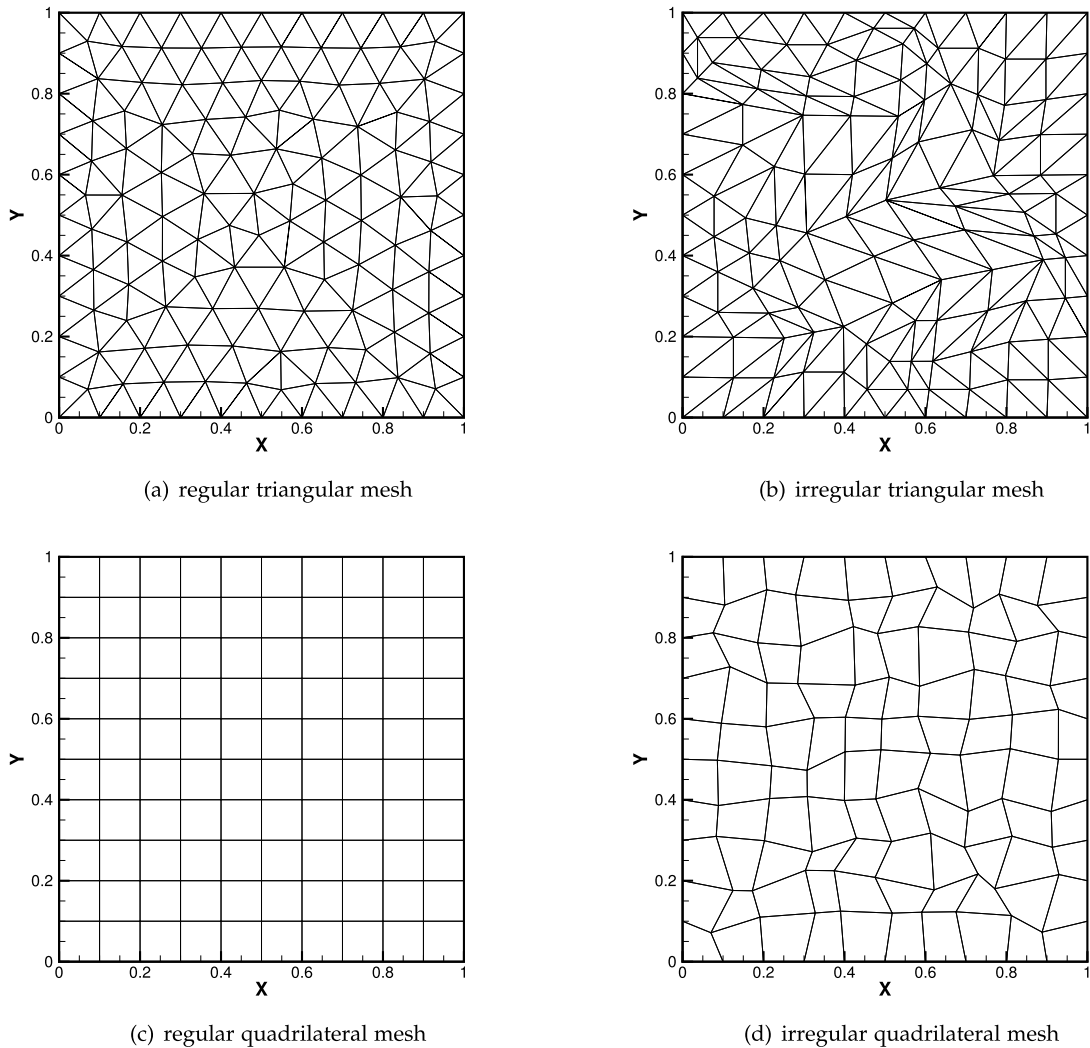


Fig. 4. Meshes with size $h = 0.1$ for the manufactured Navier–Stokes solution problem.

Table 3

Accuracy test results for the manufactured Navier–Stokes solution problem on quadrilateral meshes.

Grid size	Schemes	L_2 error	Order	L_2 error	Order
		Regular		Irregular	
1/10	2nd order FV	8.57E–03		9.12E–03	
1/20		2.56E–03	1.75	2.74E–03	1.73
1/40		7.04E–04	1.86	7.74E–04	1.82
1/80		1.85E–04	1.93	2.08E–04	1.90
1/10	4th order CLSFV	2.26E–03		3.31E–03	
1/20		9.91E–05	4.51	1.60E–04	4.37
1/40		6.89E–06	3.85	1.03E–05	3.96
1/80		5.19E–07	3.73	7.86E–07	3.71
1/10	4th order VFV	2.07E–03		2.28E–03	
1/20		2.63E–05	6.30	5.68E–05	5.33
1/40		7.66E–07	5.10	3.96E–06	3.84
1/80		4.92E–08	3.96	3.00E–07	3.72

4.2. Supersonic vortex

This test case is used to assess the accuracy of the VFV scheme in solving problems with physical boundaries and the results are compared with those computed by the same order CLSFV scheme. We consider an inviscid, isentropic and supersonic flow between two concentric circular arcs of radii $r_i = 1$ and $r_o = 1.384$ in the first quadrant. This shock-free

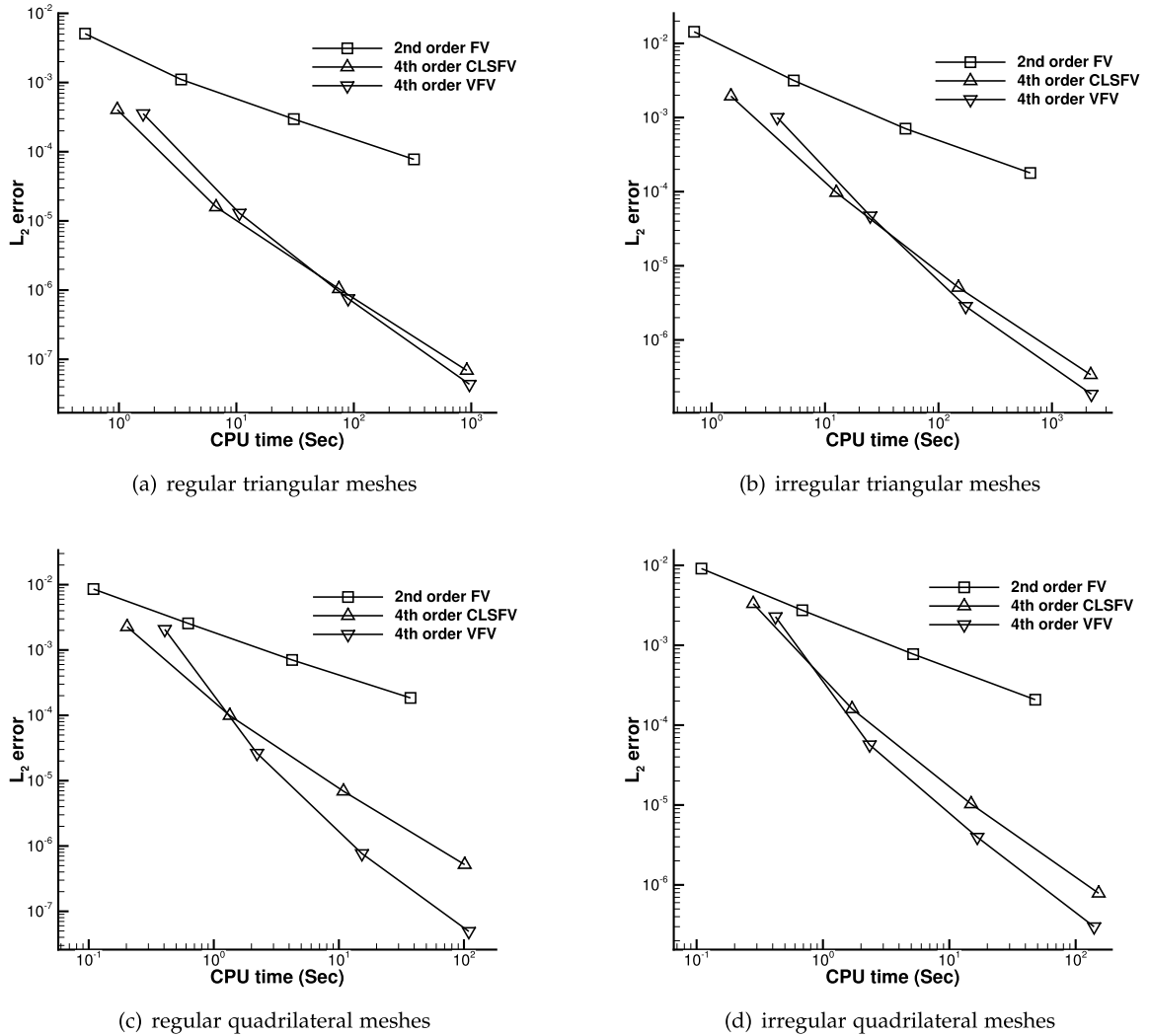


Fig. 5. Efficiency comparison for the manufactured Navier–Stokes solution problem.

compressible flow problem is widely used to measure the order of accuracy of unstructured grid methods [64,65]. The exact density in terms of radius r is given by

$$\rho = \rho_i \left\{ 1 + \frac{\gamma - 1}{2} M_i^2 \left[1 - \left(\frac{r_i}{r} \right)^2 \right] \right\}^{1/(\gamma - 1)}. \quad (54)$$

The velocity and pressure are given by

$$\|\mathbf{v}\|_2 = \frac{c_i}{r}, \quad p = \frac{\rho^r}{\gamma}, \quad (55)$$

where c_i is the speed of sound on the inner circle. The Mach number on the inner circle M_i is set to 2.25 and the density to 1.

Two sets of successively refined meshes, namely the triangular and the quadrilateral meshes, are used in the computations. The coarsest triangular and quadrilateral meshes are shown in Fig. 6. The curved boundary treatment presented in [2] is used to avoid degradation of accuracy near the boundary. The CFL number for local pseudo time step is set to 40. In each simulation, the solution is computed until the residual reaches to machine zero. The errors of density in terms of L_1 , L_2 and L_∞ norms and the rates of convergence are listed in Table 4.

The results in Table 4 show that on both triangular and quadrilateral meshes, the VFV scheme can achieve the theoretical fourth-order accuracy in terms of the L_1 , L_2 and L_∞ errors. While the CLSFV scheme achieves slightly lower than fourth-order accuracy in terms of L_1 error and can only achieve third-order accuracy in terms of L_∞ error. The VFV scheme achieves about one-order higher accuracy than the CLSFV scheme. This is because the CLSFV scheme reduces the order of

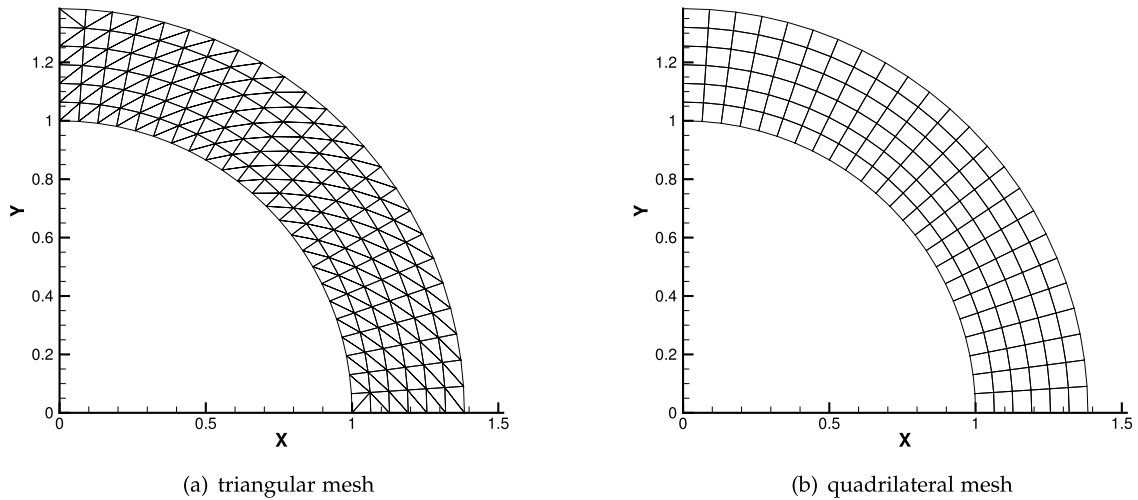


Fig. 6. Triangular and quadrilateral meshes with 25×7 grid points for the supersonic vortex problem.

Table 4

Accuracy test results for the supersonic vortex problem.

Schemes	Grid points	L_1 error	Order	L_2 error	Order	L_∞ error	Order
4th order CLSFV on triangular mesh	25×7	$3.27\text{E}-04$		$5.51\text{E}-04$		$2.12\text{E}-03$	
	49×13	$2.66\text{E}-05$	3.62	$5.64\text{E}-05$	3.29	$3.17\text{E}-04$	2.74
	97×25	$1.94\text{E}-06$	3.78	$5.31\text{E}-06$	3.41	$4.35\text{E}-05$	2.87
	193×49	$1.33\text{E}-07$	3.86	$4.83\text{E}-07$	3.46	$5.65\text{E}-06$	2.94
4th order VFV on triangular mesh	25×7	$2.84\text{E}-05$		$4.15\text{E}-05$		$1.67\text{E}-04$	
	49×13	$1.67\text{E}-06$	4.09	$3.17\text{E}-06$	3.71	$1.72\text{E}-05$	3.28
	97×25	$8.28\text{E}-08$	4.33	$1.86\text{E}-07$	4.09	$1.30\text{E}-06$	3.73
	193×49	$4.04\text{E}-09$	4.36	$9.60\text{E}-09$	4.28	$8.87\text{E}-08$	3.87
4th order CLSFV on quadrilateral mesh	25×7	$1.35\text{E}-03$		$1.73\text{E}-03$		$4.55\text{E}-03$	
	49×13	$1.78\text{E}-04$	2.92	$2.25\text{E}-04$	2.94	$8.20\text{E}-04$	2.47
	97×25	$1.77\text{E}-05$	3.33	$2.26\text{E}-05$	3.32	$1.21\text{E}-04$	2.76
	193×49	$1.46\text{E}-06$	3.60	$2.11\text{E}-06$	3.42	$1.63\text{E}-05$	2.90
4th order VFV on quadrilateral mesh	25×7	$1.38\text{E}-04$		$1.68\text{E}-04$		$3.55\text{E}-04$	
	49×13	$6.31\text{E}-06$	4.45	$7.93\text{E}-06$	4.41	$3.24\text{E}-05$	3.46
	97×25	$2.27\text{E}-07$	4.80	$3.17\text{E}-07$	4.65	$1.44\text{E}-06$	4.49
	193×49	$7.40\text{E}-09$	4.94	$1.22\text{E}-08$	4.70	$7.95\text{E}-08$	4.18

reconstruction polynomial at the boundary, while the VFV scheme uses uniform order of reconstruction polynomial in the whole computational domain. The accuracy test results demonstrate that the VFV scheme has higher accuracy than the CLSFV scheme in solving problems with physical boundaries.

4.3. Flat plate boundary layer

This test case is used to test the capability of the VFV and the CLSFV schemes to simulate viscous boundary layers, where highly clustered meshes are employed to resolve the steep velocity gradient. We consider the laminar flow over an adiabatic flat plate at a free-stream Mach number of 0.2 and a Reynolds number of 1×10^5 based on the free-stream velocity and the length of the flat plate. The plate is of the length of unity and is preceded by a slip wall of length 1.25. The Prandtl number is 0.72. The computational mesh with 140×60 stretched quadrilateral elements is shown in Fig. 7. The CFL number for local pseudo time step is 40.

The computed stream-wise and normal velocity profiles at $x = 0.5$ by the VFV and CLSFV schemes are compared with the Blasius solution in Fig. 8. The comparison shows that the numerical solutions agree with the exact solution quite well. Furthermore, the normal velocity profile computed by the VFV scheme show better agreement with the Blasius solution than that of the CLSFV scheme, which is also true for the skin-friction coefficient as shown in Fig. 9. Therefore, the proposed VFV scheme has stronger capability of resolving viscous boundary layers on highly clustered meshes than the CLSFV scheme.

4.4. Subsonic flow past a NACA0012 airfoil

This test case is used to study the convergence performance of the VFV and CLSFV schemes for both inviscid and viscous steady-state flow simulations. The second-order FV scheme is also tested to compare with the high order schemes. The

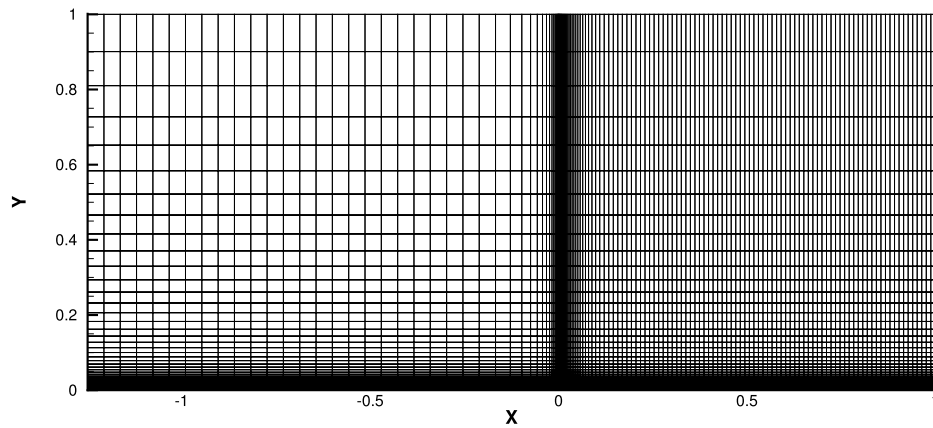


Fig. 7. Mesh for the flat plate boundary layer problem.

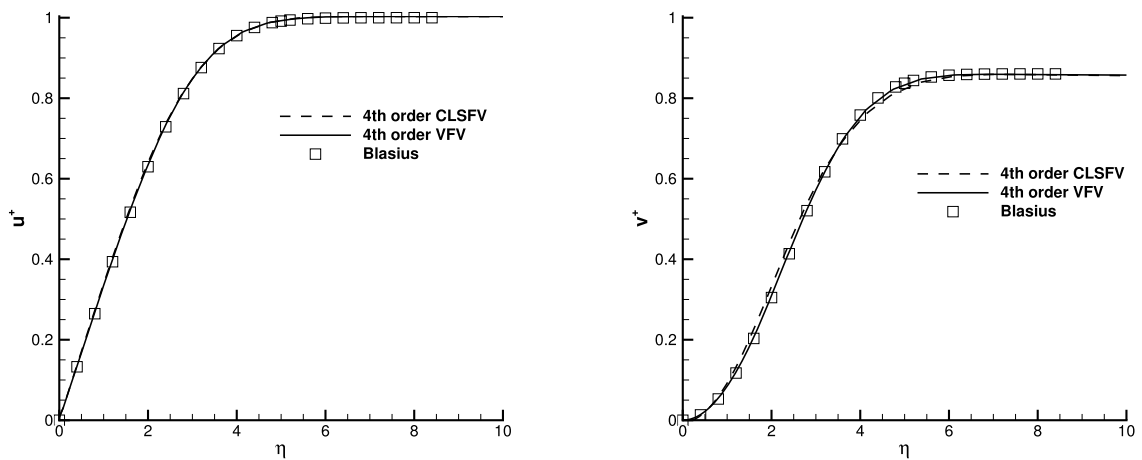


Fig. 8. Velocity profiles for the flat plate boundary layer.

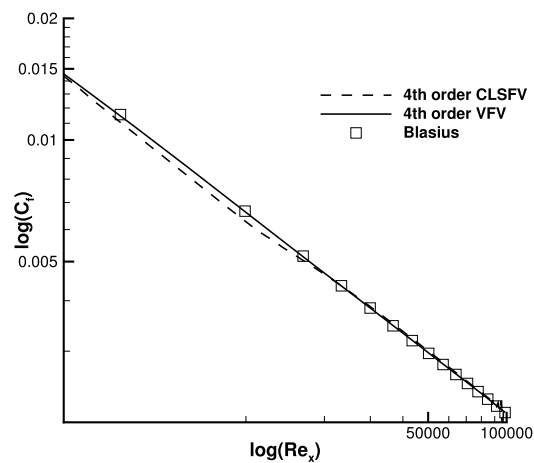


Fig. 9. Skin-friction coefficient along the flat plate.

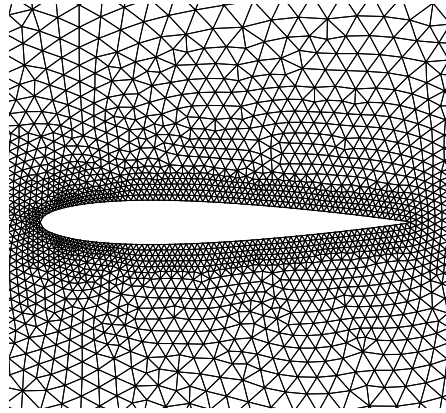


Fig. 10. Triangular mesh (nelem = 10,382, npoint = 5,306, nbound = 150) used for computing subsonic inviscid flow past a NACA0012 airfoil.

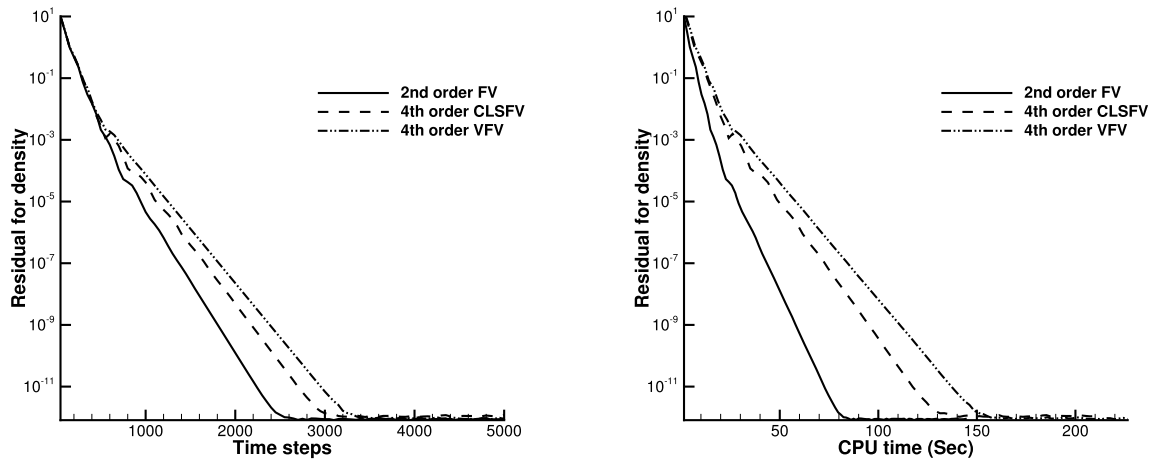


Fig. 11. Convergence history comparison for the subsonic inviscid flow past a NACA0012 airfoil.

curved boundary representation [2] is used in the computations. Two flow conditions are simulated in this test case: the subsonic inviscid flow with $Ma_\infty = 0.5$ and angle of attack $\alpha = 2^\circ$, and the subsonic viscous flow with $Ma_\infty = 0.5$ and angle of attack $\alpha = 0^\circ$. The Reynolds number (based on the chord length) for the viscous flow is $Re = 5000$. All computations are started with uniform flow. The CFL number for the local pseudo time step is 40.

The triangular mesh for the computation of the subsonic inviscid flow condition is shown in Fig. 10. The comparison of convergence histories is shown in Fig. 11. The results in Fig. 11 show that all the schemes can converge to machine zero, which demonstrates the superior convergence property of these schemes. The fourth-order VFV and CLSFV schemes use similar CPU time to reach steady-state solution, while the second-order FV scheme only needs half of the CPU time. To compare the computational efficiency of the schemes, we show the comparison of the L_2 entropy error in Fig. 12. The entropy error comparison shows that the VFV scheme can obtain much more accurate solution than that of the CLSFV scheme using slightly more CPU time, which indicates that the fourth-order VFV scheme is more efficient than the fourth-order CLSFV scheme. Again the two fourth-order schemes are much more efficient than the second-order FV scheme.

The hybrid triangular and quadrilateral mesh for the computation of the subsonic viscous flow condition is shown in Fig. 13. The computed Mach number and pressure contours by the fourth-order VFV scheme are shown in Fig. 14. The computed pressure coefficient and skin-friction coefficient along the upper and lower surface of the airfoil are shown in Fig. 15.

The comparison of convergence histories is shown in Fig. 16. The results in Fig. 16 show that all the schemes can converge to machine zero, which again demonstrates the superior convergence property of these schemes. The fourth-order VFV and CLSFV schemes use nearly the same CPU time to reach steady-state solution, while the second-order FV scheme only needs one third the CPU time. Fig. 17 shows the comparison of the computed pressure coefficient and skin-friction coefficient along the lower surface of the airfoil with the reference solution computed by the VFV method on a sufficiently refined mesh with 143360 quadrilateral elements. The comparison shows that the VFV scheme can obtain more accurate solution than that of the CLSFV scheme using the nearly the same CPU time, which indicates that the fourth-order VFV scheme is more efficient than the fourth-order CLSFV scheme. Furthermore, the solutions of the two fourth-order schemes

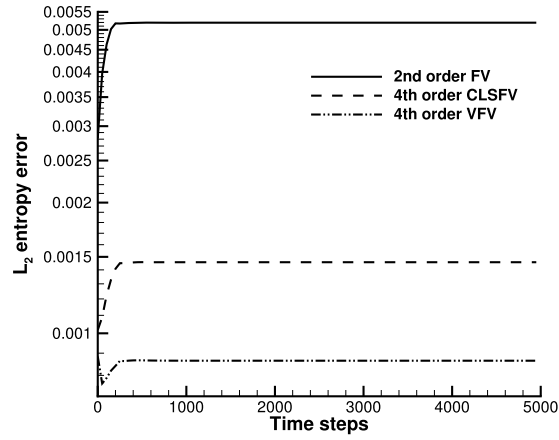


Fig. 12. Entropy error comparison for the subsonic inviscid flow past a NACA0012 airfoil.

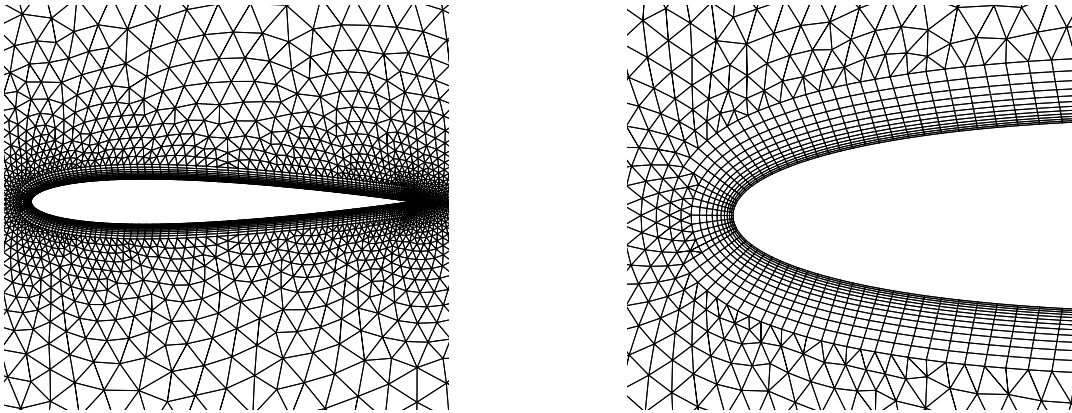


Fig. 13. Hybrid triangular and quadrilateral mesh (nelem = 9378, npoint = 5821, nbound = 174) used for computing subsonic viscous flow past a NACA0012 airfoil.

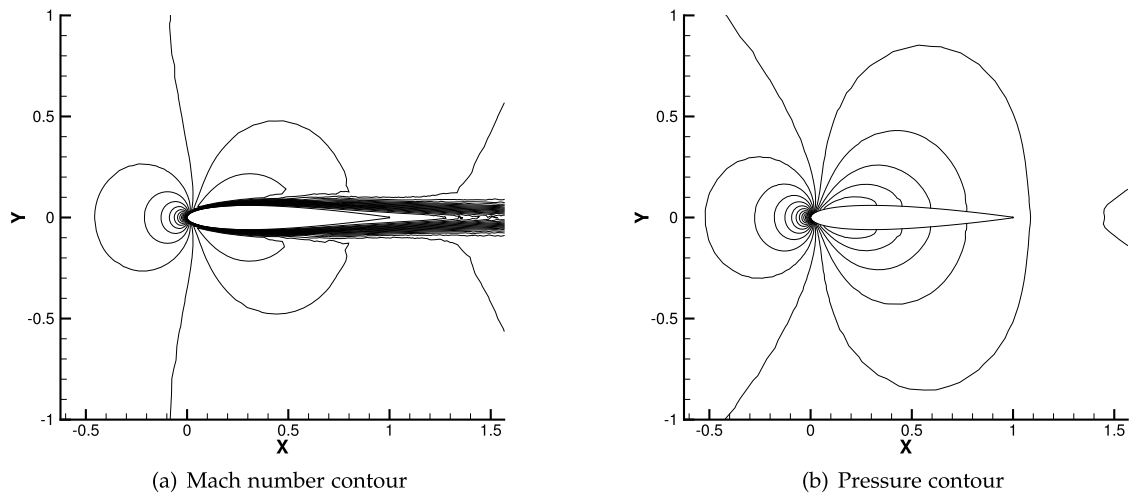


Fig. 14. Computed Mach number (left) and pressure (right) contours by the fourth-order VFV scheme for subsonic viscous flow past a NACA0012 airfoil. left: 20 equally spaced contour lines from 0.03 to 0.56; right: 20 equally spaced contour lines from 2.68 to 3.36.

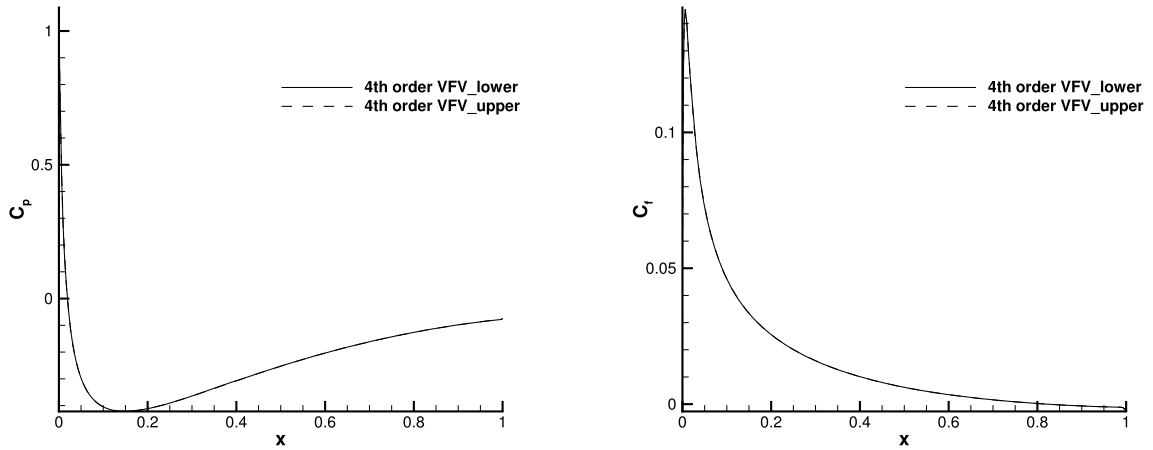


Fig. 15. Computed pressure coefficient and skin-friction coefficient curves by the fourth-order VFV scheme.

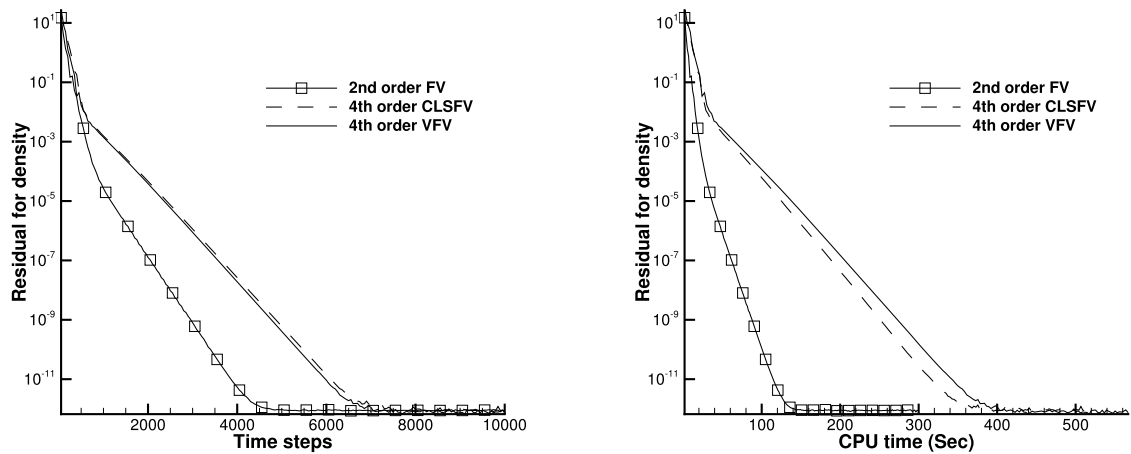


Fig. 16. Convergence history comparison for the subsonic viscous flow past a NACA0012 airfoil.

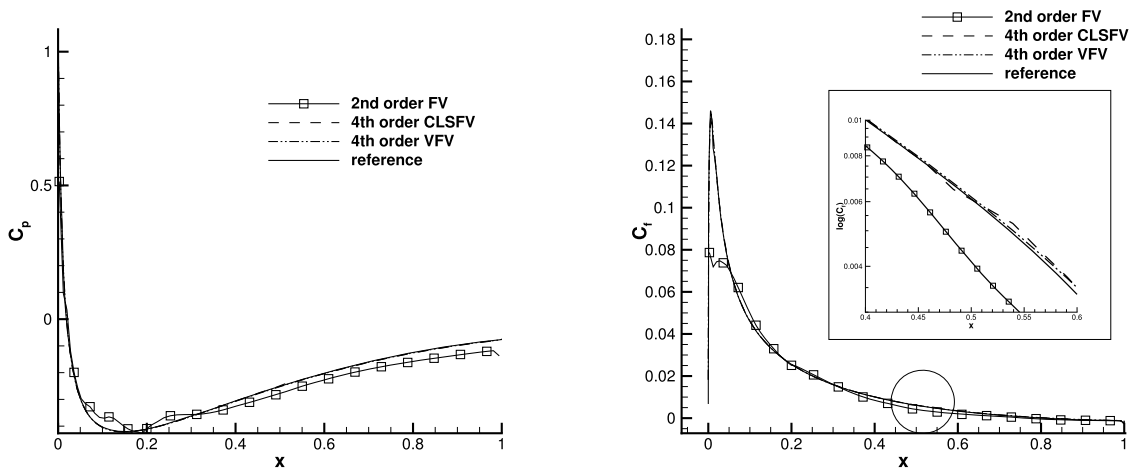


Fig. 17. Comparison of the computed pressure coefficient and skin-friction coefficient along the lower surface of the airfoil for the subsonic viscous flow past a NACA0012 airfoil.

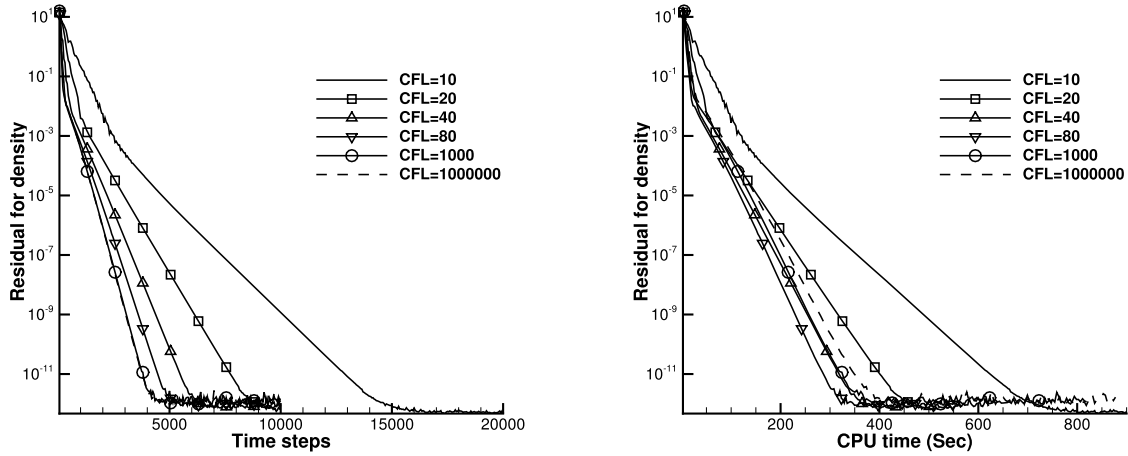


Fig. 18. Convergence history for the subsonic viscous flow past a NACA0012 airfoil problem with different CFL numbers.

show remarkably better agreement with the reference solution than the second-order FV scheme, which again demonstrate that the high order methods are much more efficient than the second-order methods.

Implementation details of the matrix-free GMRES+LU-SGS solver and a discussion of the choice of CFL number for pseudo time step are presented in the remainder of this subsection. The matrix-free LU-SGS solver is used for the left preconditioning of the approximate system of linear equations. The solution tolerance for GMRES is set to 0.1 with 10 search directions and 20 iterations. Influence of the CFL number on the computational efficiency is investigated by testing the subsonic viscous flow past a NACA0012 airfoil problem with various CFL numbers. The convergence history is shown in Fig. 18. It is shown in Fig. 18 that the larger the CFL number, the less the time steps needed to reach full convergence. While the CPU time needed to reach full convergence does not change significantly after the CFL number reaches 40. This is because more iterations are needed in the GMRES solver to satisfy the stopping criterion when using larger CFL number. The optimal CFL number is around 80 in this test case.

4.5. Shock wave impingement on a spatially evolving mixing layer

In this subsection we reproduce the example presented in [66]. This case is developed to test the behavior of the schemes for shock waves interacting with shear layers where the vortices arising from the shear layer instability are forced to pass through a shock wave. An oblique shock is made to impact on a spatially developing mixing layer at an initial convective Mach number of 0.6. The shear layer vortices pass through the shock system and later through another shock, imposed by reflection from a (slip) wall at the lower boundary. The problem has been arranged with the Mach number at the outflow boundary everywhere supersonic so that no explicit outflow boundary conditions are required. This allows us to focus on properties of the numerical schemes rather than on the boundary treatment.

Although the resulting shock wave is not strong, shock-capturing strategy is still necessary to suppress the non-physical oscillations in the vicinity of the shock wave. The problem domain is the rectangle $[0, 200] \times [-20, 20]$ with 321×81 grid points. The mesh is taken to be uniform in x direction and stretched in y direction using the method in [66].

The inflow is specified with a hyperbolic tangent profile

$$u = 2.5 + 0.5 \tanh(2y). \quad (56)$$

Therefore, the velocity of the upper stream is $u_1 = 3$, whereas the velocity of the lower stream is $u_1 = 2$. The convective Mach number, defined as $(u_1 - u_2) / (c_1 + c_2)$, where c_1 and c_2 are the free stream sound speeds, is equal to 0.6. The shear layer is excited by adding a periodic fluctuation to the vertical component of the velocity inflow given as

$$v' = \sum_{k=1}^2 a_k \cos(2\pi kt/T + \phi_k) \exp(-y^2/b), \quad (57)$$

where $b = 10$ and $T = \lambda/u_c$, wavelength $\lambda = 30$, convective velocity $u_c = (u_1 c_2 + u_2 c_1) / (c_1 + c_2) = 2.68$. For $k = 1$ we take $a_1 = 0.05$ and $\phi = 0$, and for $k = 2$ we take $a_1 = 0.05$ and $\phi = \pi/2$. No perturbations are added to the x -component of velocity. The reference density is taken as the average of the two free streams and the reference pressure is given by

$$p_R = \frac{(\rho_1 + \rho_2)(u_1 - u_2)^2}{2}. \quad (58)$$

The inflow parameters are given in [66]. The Reynolds number is 500 and the Prandtl number is 0.72.

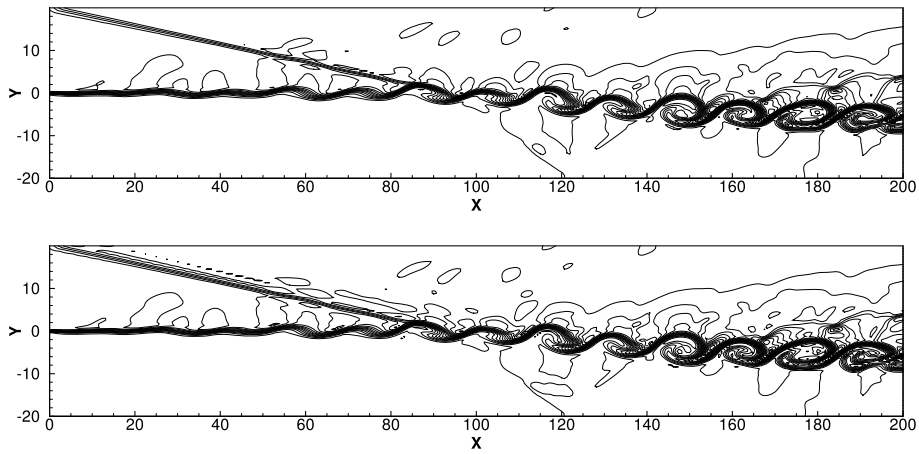


Fig. 19. Computed density contours by the CLSFV (top) and VFV (bottom) schemes for shock wave impingement on a mixing layer. 20 equally spaced contour lines from 0.4 to 2.8.

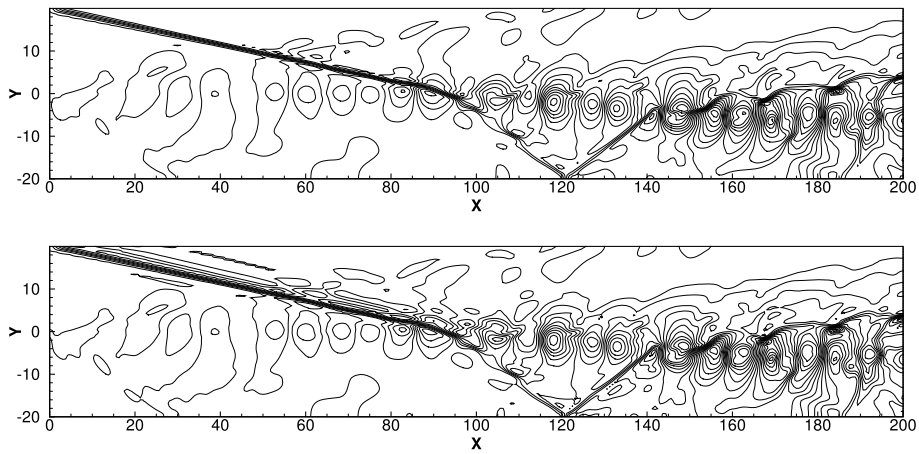


Fig. 20. Computed pressure contours by the CLSFV (top) and VFV (bottom) schemes for shock wave impingement on a mixing layer. 20 equally spaced contour lines from 0.23 to 0.73.

The problem is solved by the fourth-order VFV and CLSFV schemes until $t = 120$ using a physical time step 0.4. The CFL number for local pseudo time step is 20 and the convergence criterion for the inner iteration is that the residual decreases by 4 orders of magnitude. The VFV scheme uses 30% more CPU time than the CLSFV scheme. The computed density, pressure and temperature contours are shown in Fig. 19, Fig. 20 and Fig. 21, respectively. Both the VFV and CLSFV schemes are capable of capturing the fine scale features of the flow.

To compare the results of the two schemes intuitively, the pressure distributions along a straight line across the vortices from point (90, 0) to point (200, -6) are shown and compared with the reference solution in Fig. 22. The reference solution is computed by the fourth-order VFV scheme on a sufficiently refined mesh with 1281×321 grid points. The pressure comparison shows that the solution by the VFV scheme has larger amplitude of fluctuations, indicating that the VFV scheme is less dissipative than the CLSFV scheme.

4.6. Viscous shock tube

This test case is used to assess the resolution and shock-capturing capabilities of the VFV and CLSFV schemes. This case is characterized by interactions of strong shock waves, boundary layer and vortex. The computational domain is a squared shock tube of $[0, 1] \times [0, 1]$ with adiabatic walls. Initially, a shock wave is located at $x = 0.5$. The initial conditions are

$$(\rho_0, u_0, v_0, p_0) = \begin{cases} (120, 0, 0, 120/\gamma) & \text{for } x \leq 0.5, \\ (1.2, 0, 0, 1.2/\gamma) & \text{for } x > 0.5. \end{cases} \quad (59)$$

The shock wave, followed by a contact discontinuity, moves right to right wall. A thin boundary layer is created by the interaction of the viscous wall with the shock wave and the contact discontinuity during their propagation. Complex flow structures are then produced after the shock is reflected by the right wall.

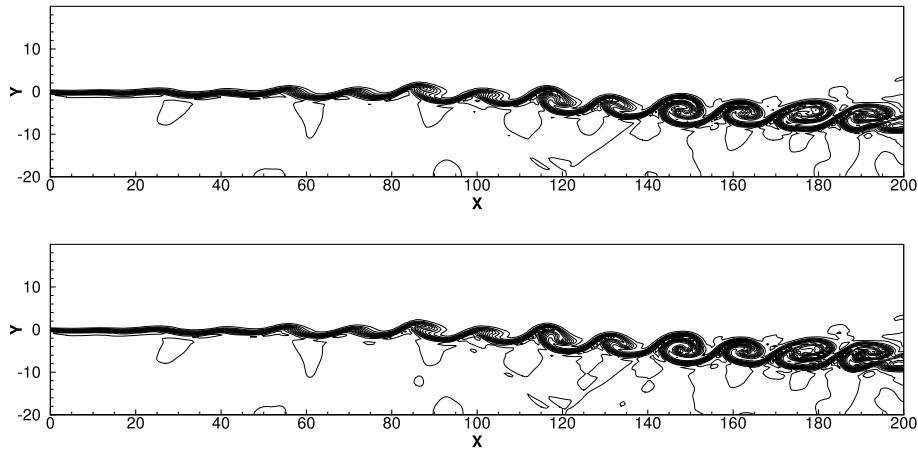


Fig. 21. Computed temperature contours by the CLSFV (top) and VFV (bottom) schemes for shock wave impingement on a mixing layer. 20 equally spaced contour lines from 0.12 to 0.7.

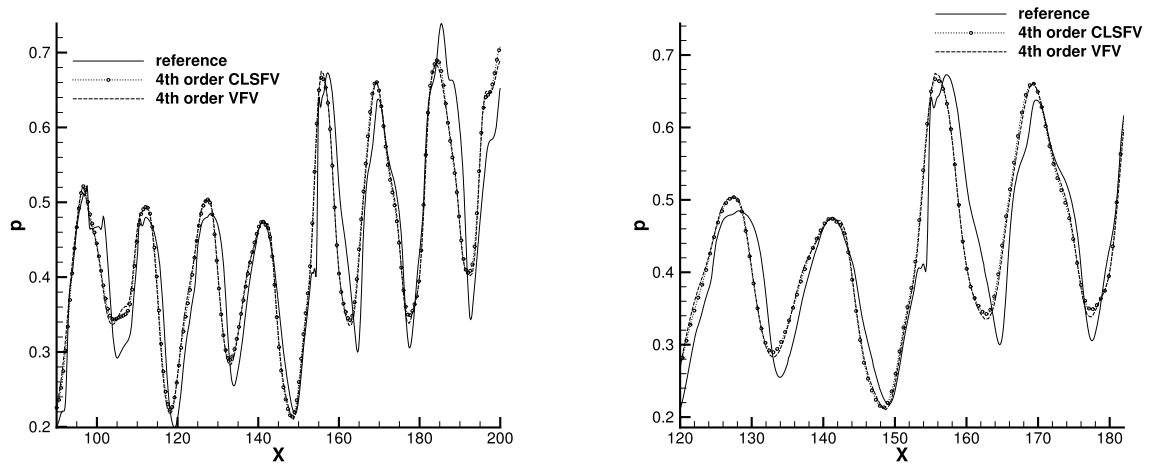


Fig. 22. Computed pressure distributions along a straight line across the vortices from point (90, 0) to point (200, -6).

Table 5

Predicted height of the primary vortex and computational cost.

Scheme	4th order CLSFV	4th order VFV	Reference
Vortex height	0.160	0.163	0.167
CPU time (sec)	18918	24338	

The Reynolds number is 200 and the Prandtl number is 0.73. The computations are performed until $t = 1$ on a uniform triangular mesh with grid size $h = 1/250$ using a physical time step $\Delta t = 0.0005$. The CFL number for local pseudo time step is 20 and the convergence criterion for the inner iteration is that the residual decreases by 3 orders of magnitude. The computed density contours by the fourth-order CLSFV and VFV schemes are shown in Fig. 23. It can be seen that all the numerical results are basically oscillation-free and the two schemes capture the complicated flow structures in high resolution. In [67], the height of the primary vortex is used to measure the grid convergence of the simulation. The height of the primary vortex and the computational cost of the simulations are listed in Table 5. The reference value of the vortex height is computed by the fourth-order VFV scheme on a sufficiently refined triangular mesh with grid size $h = 1/800$. The results in Table 5 show that the vortex height predicted by the VFV scheme is closer to the reference value and the computational cost of the VFV scheme is 29% more than the CLSFV scheme. The results demonstrate that both schemes have excellent shock-capturing capability and the VFV scheme has higher resolution than the CLSFV scheme.

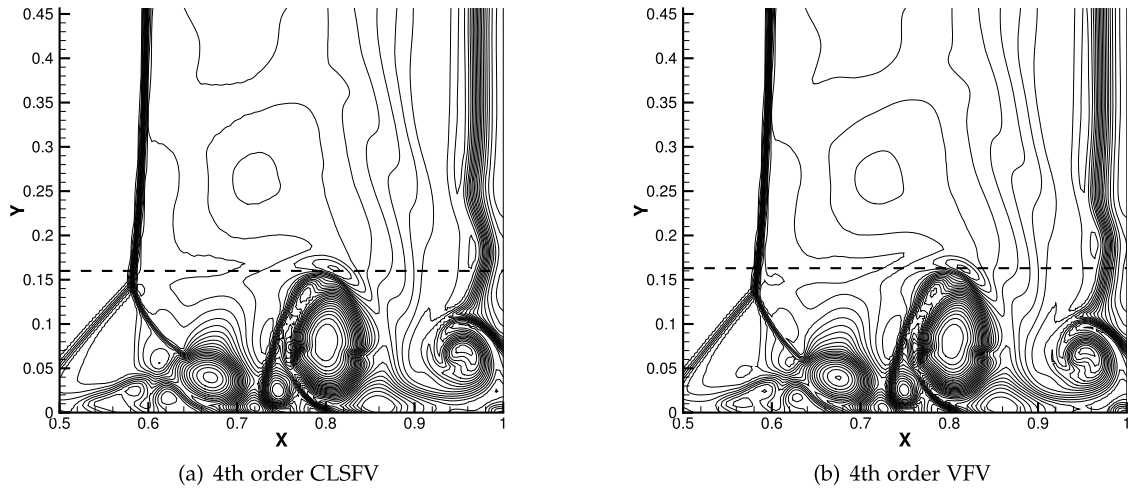


Fig. 23. Computed density contours for the viscous shock tube problem. 30 equally spaced contour lines from 22.26 to 121.34.

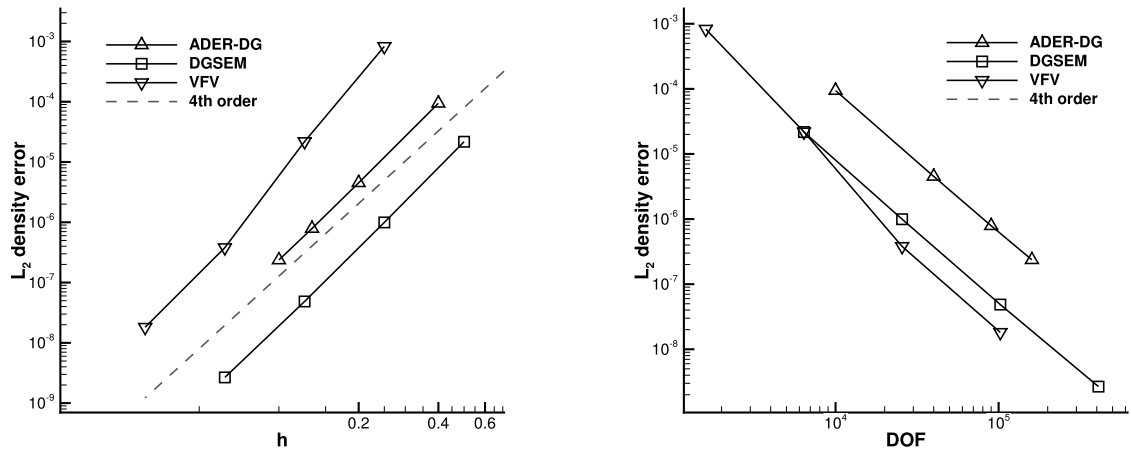


Fig. 24. Accuracy comparison for the isentropic vortex problem.

4.7. Isentropic vortex

The widely used isentropic vortex problem [33] is used here to provide comparison of accuracy between the VFV and the DG schemes. Details of the computational setup are given in [2]. The computations are performed until $t = 10$. Four successively refined regular quadrilateral meshes are used in the computations. The grid sizes are chosen to be $1/4$ to $1/32$, and the corresponding physical time steps are $1/10$ to $1/80$. The CFL number for the local pseudo time step is 100 and the convergence criterion for the inner iteration is that the residual decreases by 7 orders of magnitude.

The L_2 density errors are shown in Fig. 24. The results of the fourth-order DGSEM [68–71] and the results of [72] using the fourth-order ADER-DG method are also shown for comparison. The results in Fig. 24 show that all the schemes achieve the desired fourth-order accuracy. The two DG schemes are remarkably more accurate than the VFV scheme on the same mesh. This is not surprising since degree of freedom (DOF) of the DG schemes are 16 times as many as the VFV scheme. The results in Fig. 24 also show that, the errors of the ADER-DG, DGSEM and VFV schemes are comparable at the same DOF.

5. Conclusions

This paper presents a variational reconstruction for the high order finite volume method in solving the two-dimensional Navier–Stokes equations on arbitrary unstructured grids. In the variational reconstruction, an interfacial jump integration is defined to measure the jumps of the reconstruction polynomial and its spatial derivatives on each cell interface. The large sparse linear equation system to determine the reconstruction polynomials is obtained by minimizing the total interfacial jump integration in the computational domain using the variational method. The remarkable features of this approach are that there exists a unique solution to the reconstruction problem and the block Jacobi, Gauss–Seidel, and the SOR iterations can be proved to be convergent. The reconstruction and time integration coupled iteration method is used to achieve high

computational efficiency. A problem-independent shock detector and an improved WBAP limiter in the characteristic space are used to suppress non-physical oscillations in the simulation of flow with discontinuities. Numerical results demonstrate the high order accuracy, high computational efficiency and excellent shock-capturing capability of the finite volume method using the variational reconstruction.

Acknowledgements

This work is supported by Projects 11672160 and U1430235 of NSFC.

References

- [1] Q. Wang, Y.-X. Ren, W. Li, Compact high order finite volume method on unstructured grids I: basic formulations and one-dimensional schemes, *J. Comput. Phys.* 314 (2016) 863–882.
- [2] Q. Wang, Y.-X. Ren, W. Li, Compact high order finite volume method on unstructured grids II: extension to two-dimensional Euler equations, *J. Comput. Phys.* 314 (2016) 883–908.
- [3] W.H. Reed, T. Hill, Triangular mesh methods for the neutron transport equation, Los Alamos Report LA-UR-73-479.
- [4] B. Cockburn, C.-W. Shu, TVB Runge–Kutta local projection discontinuous Galerkin finite element method for conservation laws II: general framework, *Math. Comput.* 52 (186) (1989) 411–435.
- [5] B. Cockburn, S.-Y. Lin, C.-W. Shu, TVB Runge–Kutta local projection discontinuous Galerkin finite element method for conservation laws III: one-dimensional systems, *J. Comput. Phys.* 84 (1) (1989) 90–113.
- [6] B. Cockburn, S. Hou, C.-W. Shu, The Runge–Kutta local projection discontinuous Galerkin finite element method for conservation laws IV: the multidimensional case, *Math. Comput.* 54 (190) (1990) 545–581.
- [7] B. Cockburn, C.-W. Shu, Runge–Kutta discontinuous Galerkin methods for convection-dominated problems, *J. Sci. Comput.* 16 (3) (2001) 173–261.
- [8] M. Dumbser, D.S. Balsara, E.F. Toro, C.-D. Munz, A unified framework for the construction of one-step finite volume and discontinuous Galerkin schemes on unstructured meshes, *J. Comput. Phys.* 227 (18) (2008) 8209–8253.
- [9] M. Dumbser, O. Zanotti, Very high order PnM schemes on unstructured meshes for the resistive relativistic MHD equations, *J. Comput. Phys.* 228 (18) (2009) 6991–7006.
- [10] M. Dumbser, Arbitrary high order PnM schemes on unstructured meshes for the compressible Navier–Stokes equations, *Comput. Fluids* 39 (1) (2010) 60–76.
- [11] H. Luo, L. Luo, R. Nourgaliev, V.A. Mousseau, N. Dinh, A reconstructed discontinuous Galerkin method for the compressible Navier–Stokes equations on arbitrary grids, *J. Comput. Phys.* 229 (19) (2010) 6961–6978.
- [12] H. Luo, Y. Xia, S. Spiegel, R. Nourgaliev, Z. Jiang, A reconstructed discontinuous Galerkin method based on a hierarchical WENO reconstruction for compressible flows on tetrahedral grids, *J. Comput. Phys.* 236 (2013) 477–492.
- [13] L. Zhang, W. Liu, L. He, X. Deng, H. Zhang, A class of hybrid DG/FV methods for conservation laws I: basic formulation and one-dimensional systems, *J. Comput. Phys.* 231 (4) (2012) 1081–1103.
- [14] L. Zhang, W. Liu, L. He, X. Deng, H. Zhang, A class of hybrid DG/FV methods for conservation laws II: two-dimensional cases, *J. Comput. Phys.* 231 (4) (2012) 1104–1120.
- [15] R. Abgrall, M. Mezone, Construction of second order accurate monotone and stable residual distribution schemes for unsteady flow problems, *J. Comput. Phys.* 188 (1) (2003) 16–55.
- [16] M. Ricchiuto, Á. Csík, H. Deconinck, Residual distribution for general time-dependent conservation laws, *J. Comput. Phys.* 209 (1) (2005) 249–289.
- [17] R. Abgrall, Residual distribution schemes: current status and future trends, *Comput. Fluids* 35 (7) (2006) 641–669.
- [18] R. Abgrall, A. Larat, M. Ricchiuto, Construction of very high order residual distribution schemes for steady inviscid flow problems on hybrid unstructured meshes, *J. Comput. Phys.* 230 (11) (2011) 4103–4136.
- [19] Z.J. Wang, Spectral (finite) volume method for conservation laws on unstructured grids: basic formulation, *J. Comput. Phys.* 178 (1) (2002) 210–251.
- [20] Z.J. Wang, Y. Liu, Spectral (finite) volume method for conservation laws on unstructured grids II: extension to two-dimensional scalar equation, *J. Comput. Phys.* 179 (2) (2002) 665–697.
- [21] Z.J. Wang, Y. Liu, Spectral (finite) volume method for conservation laws on unstructured grids III: one dimensional systems and partition optimization, *J. Sci. Comput.* 20 (1) (2004) 137–157.
- [22] Z.J. Wang, L. Zhang, Y. Liu, Spectral (finite) volume method for conservation laws on unstructured grids IV: extension to two-dimensional systems, *J. Comput. Phys.* 194 (2) (2004) 716–741.
- [23] Y. Liu, M. Vinokur, Z. Wang, Spectral difference method for unstructured grids I: basic formulation, *J. Comput. Phys.* 216 (2) (2006) 780–801.
- [24] Z. Wang, Y. Liu, G. May, A. Jameson, Spectral difference method for unstructured grids II: extension to the Euler equations, *J. Sci. Comput.* 32 (1) (2007) 45–71.
- [25] G. May, A. Jameson, A spectral difference method for the Euler and Navier–Stokes equations on unstructured meshes, AIAA paper 304, 2006, pp. 1–18.
- [26] H. Huynh, A flux reconstruction approach to high-order schemes including discontinuous Galerkin methods, AIAA paper 4079, 2007, pp. 1–42.
- [27] Z. Wang, H. Gao, A unifying lifting collocation penalty formulation including the discontinuous Galerkin, spectral volume/difference methods for conservation laws on mixed grids, *J. Comput. Phys.* 228 (21) (2009) 8161–8186.
- [28] T.J. Barth, P.O. Frederickson, Higher order solution of the Euler equations on unstructured grids using quadratic reconstruction, AIAA paper 0013, 1990, pp. 1–8.
- [29] M. Delanaye, Quadratic reconstruction finite volume schemes on 3D Arbitrary unstructured polyhedral grids, AIAA paper 3259, 1989, pp. 80–90.
- [30] C.F. Ollivier-Gooch, Quasi-ENO schemes for unstructured meshes based on unlimited data-dependent least-squares reconstruction, *J. Comput. Phys.* 133 (1) (1997) 6–17.
- [31] C. Ollivier-Gooch, M. Van Altena, A high-order-accurate unstructured mesh finite-volume scheme for the advection–diffusion equation, *J. Comput. Phys.* 181 (2) (2002) 729–752.
- [32] O. Friedrich, Weighted essentially non-oscillatory schemes for the interpolation of mean values on unstructured grids, *J. Comput. Phys.* 144 (1) (1998) 194–212.
- [33] C. Hu, C.-W. Shu, Weighted essentially non-oscillatory schemes on triangular meshes, *J. Comput. Phys.* 150 (1) (1999) 97–127.
- [34] M. Dumbser, M. Käser, Arbitrary high order non-oscillatory finite volume schemes on unstructured meshes for linear hyperbolic systems, *J. Comput. Phys.* 221 (2) (2007) 693–723.
- [35] M. Dumbser, M. Käser, V.A. Titarev, E.F. Toro, Quadrature-free non-oscillatory finite volume schemes on unstructured meshes for nonlinear hyperbolic systems, *J. Comput. Phys.* 226 (1) (2007) 204–243.

- [36] Z. Sun, S. Inaba, F. Xiao, Boundary variation diminishing (BVD) reconstruction: a new approach to improve Godunov scheme, *J. Comput. Phys.* 322 (2016) 309–325.
- [37] F. Haider, J.-P. Croisille, B. Courbet, Stability analysis of the cell centered finite-volume MUSCL method on unstructured grids, *Numer. Math.* 113 (4) (2009) 555–600.
- [38] R. Abgrall, On essentially non-oscillatory schemes on unstructured meshes: analysis and implementation, *J. Comput. Phys.* 114 (1994) 45–58.
- [39] H. Luo, J.D. Baum, R. Löhner, A discontinuous Galerkin method based on a Taylor basis for the compressible flows on arbitrary grids, *J. Comput. Phys.* 227 (20) (2008) 8875–8893.
- [40] W. Hackbusch, *Iterative Solution of Large Sparse Systems of Equations*, vol. 95, Springer Science & Business Media, 2012.
- [41] A. Arnone, M.-S. Liou, L.A. Povinelli, Integration of Navier–Stokes equations using dual time stepping and a multigrid method, *AIAA J.* 33 (6) (1995) 985–990.
- [42] L. Zhang, Z. Wang, A block LU-SGS implicit dual time-stepping algorithm for hybrid dynamic meshes, *Comput. Fluids* 33 (7) (2004) 891–916.
- [43] H. Luo, J.D. Baum, R. Löhner, A fast, matrix-free implicit method for compressible flows on unstructured grids, *J. Comput. Phys.* 146 (2) (1998) 664–690.
- [44] L. Ferracina, M. Spijker, Strong stability of singly-diagonally-implicit Runge–Kutta methods, *Appl. Numer. Math.* 58 (11) (2008) 1675–1686.
- [45] S.K. Lele, Compact finite difference schemes with spectral-like resolution, *J. Comput. Phys.* 103 (1) (1992) 16–42.
- [46] C.-W. Shu, S. Osher, Efficient implementation of essentially non-oscillatory shock-capturing schemes, *J. Comput. Phys.* 77 (2) (1988) 439–471.
- [47] P. Rasetarinera, M. Hussaini, An efficient implicit discontinuous spectral Galerkin method, *J. Comput. Phys.* 172 (2) (2001) 718–738.
- [48] L.T. Diodady, D.L. Darmofal, Preconditioning methods for discontinuous Galerkin solutions of the Navier–Stokes equations, *J. Comput. Phys.* 228 (11) (2009) 3917–3935.
- [49] X. Yang, J. Cheng, C. Wang, H. Luo, J. Si, A. Pandare, A fast, implicit discontinuous Galerkin method based on analytical Jacobians for the compressible Navier–Stokes equations, in: 54th AIAA Aerospace Sciences Meeting, 2016, p. 1326.
- [50] W. Li, Y.-X. Ren, High-order k-exact WENO finite volume schemes for solving gas dynamic Euler equations on unstructured grids, *Int. J. Numer. Methods Fluids* 70 (6) (2012) 742–763.
- [51] W. Li, Y.-X. Ren, G. Lei, H. Luo, The multi-dimensional limiters for solving hyperbolic conservation laws on unstructured grids, *J. Comput. Phys.* 230 (21) (2011) 7775–7795.
- [52] W. Li, Y.-X. Ren, The multi-dimensional limiters for solving hyperbolic conservation laws on unstructured grids II: extension to high order finite volume schemes, *J. Comput. Phys.* 231 (11) (2012) 4053–4077.
- [53] P. Roe, J. Pike, Efficient construction and utilisation of approximate Riemann solutions, in: *Proc. of the Sixth Int'l. Symposium on Computing Methods in Applied Sciences and Engineering*, VI, North-Holland Publishing Co., 1985, pp. 499–518.
- [54] P.L. Roe, Approximate Riemann solvers, parameter vectors, and difference schemes, *J. Comput. Phys.* 43 (2) (1981) 357–372.
- [55] R. Sanders, E. Morano, M.-C. Druguet, Multidimensional dissipation for upwind schemes: stability and applications to gas dynamics, *J. Comput. Phys.* 145 (2) (1998) 511–537.
- [56] G. Mengaldo, D. De Grazia, J. Peiro, A. Farrington, F. Witherden, P. Vincent, S. Sherwin, A guide to the implementation of boundary conditions in compact high-order methods for compressible aerodynamics, in: 7th AIAA Theoretical Fluid Mechanics Conference, AIAA Aviation, American Institute of Aeronautics and Astronautics, 2014.
- [57] G. Gassner, F. Lörcher, C.-D. Munz, A contribution to the construction of diffusion fluxes for finite volume and discontinuous Galerkin schemes, *J. Comput. Phys.* 224 (2) (2007) 1049–1063.
- [58] R. Hartmann, P. Houston, Symmetric interior penalty DG methods for the compressible Navier–Stokes equations I: method formulation, *Int. J. Numer. Anal. Model.* 3 (2006) 1–20.
- [59] G. Gassner, F. Lörcher, C.-D. Munz, A discontinuous Galerkin scheme based on a space-time expansion II: viscous flow equations in multi dimensions, *J. Sci. Comput.* 34 (3) (2008) 260–286.
- [60] H. Nishikawa, Beyond interface gradient: a general principle for constructing diffusion schemes, in: *Proc. of 40th AIAA Fluid Dynamics Conference and Exhibit*, 2010.
- [61] A. Jalali, M. Sharbatdar, C. Olivier-Gooch, Accuracy analysis of unstructured finite volume discretization schemes for diffusive fluxes, *Comput. Fluids* 101 (2014) 220–232.
- [62] W. Li, Y.-X. Ren, The multi-dimensional limiters for discontinuous Galerkin method on unstructured grids, *Comput. Fluids* 96 (2014) 368–376.
- [63] Z. Wang, K. Fidkowski, R. Abgrall, F. Bassi, D. Caraeni, A. Cary, H. Deconinck, R. Hartmann, K. Hillewaert, H. Huynh, et al., High-order CFD methods: current status and perspective, *Int. J. Numer. Methods Fluids* 72 (8) (2013) 811–845.
- [64] M. Aftosmis, D. Gaitonde, T.S. Tavares, Behavior of linear reconstruction techniques on unstructured meshes, *AIAA J.* 33 (11) (1995) 2038–2049.
- [65] L. Krivodonova, M. Berger, High-order accurate implementation of solid wall boundary conditions in curved geometries, *J. Comput. Phys.* 211 (2) (2006) 492–512.
- [66] H.C. Yee, N.D. Sandham, M. Djomehri, Low-dissipative high-order shock-capturing methods using characteristic-based filters, *J. Comput. Phys.* 150 (1) (1999) 199–238.
- [67] V. Daru, C. Tenaud, Evaluation of TVD high resolution schemes for unsteady viscous shocked flows, *Comput. Fluids* 30 (1) (2000) 89–113.
- [68] D.A. Kopriva, G. Gassner, On the quadrature and weak form choices in collocation type discontinuous Galerkin spectral element methods, *J. Sci. Comput.* 44 (2) (2010) 136–155.
- [69] C.A.A. Minoli, D.A. Kopriva, Discontinuous Galerkin spectral element approximations on moving meshes, *J. Comput. Phys.* 230 (5) (2011) 1876–1902.
- [70] A.D. Beck, T. Bolemann, D. Flad, H. Frank, G.J. Gassner, F. Hindenlang, C.-D. Munz, High-order discontinuous Galerkin spectral element methods for transitional and turbulent flow simulations, *Int. J. Numer. Methods Fluids* 76 (8) (2014) 522–548.
- [71] D. Flad, A. Beck, C.-D. Munz, Simulation of underresolved turbulent flows by adaptive filtering using the high order discontinuous Galerkin spectral element method, *J. Comput. Phys.* 313 (2016) 1–12.
- [72] M. Dumbser, O. Zanotti, R. Loubère, S. Diot, A posteriori subcell limiting of the discontinuous Galerkin finite element method for hyperbolic conservation laws, *J. Comput. Phys.* 278 (2014) 47–75.